High-speed pullout behavior of deep-mounted cfrp strips bonded with a flexible adhesive to clay brick masonry

Ö.S. Türkmen[a,*], S.N.M. Wijte[a], J. Vaculik[b], B.T. De Vries[c], J.M. Ingham[d]

[a] Department of the Built Environment, Section Structural Design, Eindhoven University of Technology, P.O. Box 513, 5600 MB Eindhoven, the Netherlands
[b] School of Civil, Environmental and Mining Engineering, The University of Adelaide, SA 5005, Australia
[c] QuakeShield (joint venture Royal Oosterhof Holman and SealteQ Group), P.O. Box 6, 9843 ZG Grijpskerk, the Netherlands
[d] Department of Civil and Environmental Engineering, University of Auckland, 92019 Auckland, New Zealand

ARTICLE INFO

ABSTRACT

An experimental campaign was initiated to determine the high-speed pullout behavior of deep-mounted carbon fibre-reinforced polymer (CFRP) strips bonded with a flexible, visco-elasto-plastic adhesive to clay brick masonry. A total of 14 direct pull-tests were conducted. Strong correlations were found between both the pull-out strength/bonded length relation and the pull-out strength/loading rate relation. The governing failure mechanism was either cohesive failure combined with brick splitting, or CFRP rupture without significant damage to the masonry prism. From the strain gauge readings, multiple bond-slip correlations were constructed and eventually generalized and simplified to a global, multi-linear bond-slip relation. Using the global bond-slip law as part of a partial-interaction analysis resulted in a good fit with the experimental results. Finally, the results of this study were compared to previous direct pull-tests found in literature, showing that the application of a flexible adhesive results in higher interfacial fracture energy and higher debonding slip.

1. Introduction

There is a growing awareness worldwide of the need to seismically improve the existing building stock to protect communities in the event of future earthquakes. This development, mainly driven by the need to warrant a sufficient level of safety, has led to the broad use of fibre-reinforced polymer (FRP) as retrofit material. The deep mounting of CFRP strips to masonry using a flexible adhesive was developed as a minimally-invasive and cost-effective out-of-plane seismic retrofitting technique for clay brick unreinforced masonry (URM) buildings. The effectiveness of this strengthening system was examined in depth in this study by means of (high-speed) direct pull-tests, as limited knowledge is available on the governing mechanics of CFRP strips mounted with a flexible, visco-elasto-plastic adhesive.

Extensive gas production has led to the occurrence of hundreds of earthquakes in Groningen. More than five decades of depletion of hydrocarbon gas within the reservoir pore space has caused the reservoir to compact, increasing the mechanical stresses on pre-existing geological faults. When the shear traction at these faults becomes sufficient to overcome frictional resistance on the fault surface, fault slip occurs leading to seismic events [18]. In contrast to tectonic earthquakes,

these induced earthquakes occur at a relative shallow depth of approximately 3 km beneath the earth's surface, and therefore have a large impact on the existing building stock despite their maximum magnitude of 3.5. The building stock in the region comprises mainly single and two-storey unreinforced masonry buildings designed without any seismic considerations, and consequently highly susceptible to earthquake events. The façades of these buildings typically consists of cavity walls with masonry leaves of 100 mm in thickness divided by a 30–80 mm wide cavity. Generally the inner leaf is constructed from either clay brick masonry or calcium silicate masonry, while clay brick masonry is most commonly used for the outer leaf. The slenderness of the load-bearing inner leaf is one of the reasons why these buildings are highly vulnerable to seismic actions. Seismic retrofitting of the unreinforced masonry walls within these buildings is crucial to mitigate the risk of collapse with likely casualties. Improvement of the out-of-plane bending performance of walls is considered most crucial [13,5,10] because out-of-plane failure is triggered by lower levels of excitation.

In the past decades, a range of strengthening techniques have been developed for enhancing the out-of-plane performance of unreinforced masonry walls. One technique involves the use of FRP composites.

* Corresponding author.
E-mail addresses: o.s.turkmen@tue.nl (Ö.S. Türkmen), s.n.m.wijte@tue.nl (S.N.M. Wijte), jaroslav.vaculik@adelaide.edu.au (J. Vaculik), bdevries@quakeshield.com (B.T. De Vries), J.Ingham@auckland.ac.nz (J.M. Ingham).

Nomenclature

b_p	width of the CFRP strip (mm)
E	Young's Modulus (N/mm^2)
f_c	uniaxial compressive strength (N/mm^2)
f_{fl}	flexural strength (N/mm^2)
f_{st}	splitting tensile strength (N/mm^2)
f_t	tensile strength (N/mm^2)
F	pull-out force (kN)
F_{end}	pull-out force at the end of the experiment (kN)
G	shear modulus (N/mm^2)
G_f	interfacial fracture energy (N/mm)
k_1	slope of the elastic zone for the local τ-δ relation (N/mm^3)
k_2	slope of the damage development zone for the local τ-δ relation (N/mm^3)
k_{ini}	initial stiffness, determined as the secant modulus at 35% of the pull-out strength (kN/mm)
L	bonded length (mm)
L_{crit}	critical bond length (mm)
L_{per}	perimeter of the failure plane (mm)
P_{max}	pull-out strength (kN)
t_p	thickness of the CFRP strip (mm)
T_p	tensile strength CFRP strip (kN)
γ_{ult}	ultimate shear strain (N/mm^2)
δ_0	free-end slip (mm)
δ_1	local slip corresponding to the end of the elastic zone (mm)
δ_2	local slip corresponding to the start of the damage development zone (mm)
δ_3	local slip corresponding to the start of the residual zone (mm)
$\delta_{L,max}$	loaded-end slip corresponding to the pull-out strength (mm)
$\delta_{L,end}$	loaded-end slip corresponding to residual pull-out load (mm)
$\dot{\delta}$	slip rate (mm/s)
$\dot{\delta}_{L,ini}$	initial loaded-end slip rate, determined as the mean up to and including 35% of the pull-out strength (mm/s)
ε	strain (%)
ϵ_{ult}	ultimate tensile strain (%)
$\dot{\varepsilon}$	strain rate (%/s)
ν	Poisson ratio (−)
ρ	density (kg/m^3)
τ	shear stress (N/mm^2)
τ_f	peak local bond stress (N/mm^2)
τ_{max}	shear strength (N/mm^2)
τ_r	residual shear stress (N/mm^2)
φ_f	depth-to-width aspect ratio of the failure plane (−)

Generally, these materials are made of carbon (CFRP), glass (GFRP), basalt (BFRP) or aramid (AFRP) fibres bonded together by epoxy resin. The main advantages of FRP include high strength, high stiffness, low weight, and immunity to corrosion [12]. Moreover in contrast to traditional strengthening methods, such as reinforced concrete jacketing and steel frames, FRP-based strengthening methods do not add considerable mass to the structure, do not alter the aesthetics of a building, and are less labor intensive [26]. Typically FRP sheets or plates are externally bonded (EB) to the masonry surface to increase both the wall's strength and ductility. The near-surface-mounted (NSM) technique has been raised as an alternative, where FRP strips or rods are inserted into shallow grooves inside the masonry and bonded to the substrate by a stiff epoxy. The advantages of this method over the EB method include significantly higher strengths, reduced aesthetic impact, reduced installation time, and superior protection from environmental influences [6,30]. However, a disadvantage of both techniques is that double-sided application is required for seismic retrofitting of masonry walls for both out-of-plane loading directions. Under typical retrofit configurations, the failure of retrofitted sections typically occurs by the mechanism of interfacial debonding, which involves fracture of the substrate adjacent to the bonded interface at a strain significantly lower than the FRP rupture strain [22]. This observation led to the development of the flexible deep mounted (FDM) technique where deeper grooves are cut in the masonry, after which FRP strips are installed inside the center of the wall, thus reinforcing the wall for both out-of-plane loading directions. To account for the previously mentioned failure of the substrate and consequent underutilization of the FRP, a flexible adhesive instead of a conventional stiff epoxy is used for bonding the FRP to the masonry substrate. It should be noted that the FDM retrofit concept was developed for solid clay brick masonry. Additional aspects such as the presence of proper wall ties need to be taken into account in order to prevent out-of-plane failure of the outer leaf of cavity walls.

Previously conducted beam tests have already demonstrated the potential of this novel strengthening system in increasing the flexural capacity of clay-brick masonry [24], and these experimental results formed the basis of a preliminary analytical model for predicting the out-of-plane behavior [31]. However, the effectiveness of any FRP retrofit system largely depends on the ability to develop shear transfer across the FRP-to-masonry bond [27], and it is thus considered essential to investigate the bond behavior of masonry retrofitted with FDM CFRP strips. The strength of the FRP-to-masonry bond depends on the following parameters: the groove and the strip dimensions, the tensile and shear strength of masonry and adhesive, the level of preparation of the groove substrate, and the position of the FRP strip within the member being strengthened [6]. The direct pull-test is the most common method to study this bond behavior, where an increasing slip is applied to the FRP until failure of the specimen occurs. As a first step towards this objective Türkmen et al. [25] conducted pull tests on various types of specimens, investigating the influence of adhesive type, strip surface treatment and groove width, to find an optimal configuration for FDM CFRP reinforcement of clay-brick masonry. The adhesive used in this study to mount the CFRP strips to the masonry prisms had a Young's modulus of less than 40 N/mm^2.

Vaculik et al. [29] collated a database from various experimental campaigns investigating the FRP-to-masonry bond strength through shear pull-tests. Looking at all 92 direct pull tests on masonry prisms with NSM CFRP strips in the aforementioned database, the minimum value of the Young's modulus of the adhesives used was 2000 N/mm^2 [17,21,32,16,6]. The pull-out test conducted by Türkmen et al. [25] showed that, despite a groove depth of 65% of the brick thickness, no premature cracking was observed, while comparable research on FRP systems with conventional epoxies showed that intermediate cracking was the leading failure mechanism at groove depths of only 30% of the brick thickness [6]. Moreover, the test results from Türkmen et al. [25] showed a near-uniform distribution of the bond over an embedded length of the CFRP strip of one meter. The added value of flexible adhesives for EB FRP on clay brick masonry units was also reported by Kwiecień [19]. These tests demonstrated that shear stress concentrations became reduced by the flexibility of the adhesive layer, significantly increasing the ultimate load and slip at failure, and further protecting the brittle substrate against locally acting peak stress. Due to visco-elasto-plastic properties of the flexible adhesive, the bond behavior of the system was strain-rate-dependent and therefore might perform better at higher loading rates [25].

The pilot study conducted by Türkmen et al. [25] showed promising

results for the pull-out behavior of deep-mounted CFRP strips bonded with a flexible adhesive to clay brick masonry. The potentially higher fracture energy and larger slip at debonding when compared to conventional stiff-adhesive systems stimulates the need for further research on the governing mechanics of the flexible adhesive in the aforementioned retrofit setting. This is considered in far greater detail in the current study by means of 14 direct pull-tests on reinforced masonry prisms. In order to investigate the influence of the embedded length of the FRP strip on the pull-out strength and the initial stiffness, four different specimen lengths were tested. To utilize the strain-dependent properties of the system, the vast majority of the specimens were tested under a high loading speed, resembling the pull-out speed during a seismic event. The effect of loading speed on the bond strength and the occurring failure mechanism is also studied. Moreover, an analytical model is elaborated to describe the force-slip behavior of the retrofit system. Finally, an extensive comparison, both for the bond-slip and the force-slip relationships, is made with previous tests on masonry specimens retrofitted with NSM FRP strips embedded in stiff epoxy.

2. Experimental program

2.1. Material characterization

The clay bricks used in this research had dimensions of $205(\pm 4) \times 95(\pm 2) \times 50(\pm 2)$ mm^3 ($l_b \times w_b \times h_b$). Mechanical characteristics of the clay bricks were determined using standard tests in accordance with the relevant standards. The bricks had a mean compressive strength of 31.7 N/mm^2. The compressive strength of the clay bricks was determined in accordance with *EN 772-1 (2011/ A1:2015)* on half brick specimens with gypsum capping. The mean splitting tensile strength (*ASTM C1006-07, 2007)* and flexural tensile strength (*ASTM C67-03, 2003*) of the bricks were 3.3 N/mm^2 and 5.89 N/mm^2, respectively. The mean flexural tensile strength of the mortar specimens was 3.6 N/mm^2, and the mean compressive strength of the mortar was 10.6 N/mm^2. Both the flexural tensile strength and the compressive strength of the mortar specimens were determined according to EN 1015-11 (1999/A1:2006). Compression tests were performed on three masonry specimens, consisting of 6-brick high bond stacked masonry prisms, under displacement control with a loading speed of 0.20 mm/min. The mean compressive strength (f_c) of the specimens was 14.8 N/mm^2. The Young's modulus was determined as a secant modulus at 35% of the compressive strength in accordance with *EN 1052-1 (1999)*. The mean Young's modulus of the masonry prims was 3100 N/mm^2. The mechanical properties of the building materials are summarized in Table 1. The coefficients of variation encountered in the materials testing program were within typically encountered bounds.

The prefabricated (pultruded) CFRP strips were 20 mm in width and 1.4 mm in thickness, with a fibre volume content of higher than 68%. The Young's modulus, tensile strength and elongation at rupture of the CFRP strip as provided by the supplier were 215 kN/mm^2, 2876 N/mm^2 and 1.59% respectively.

The material properties for the flexible adhesive under tension (mode I loading) were obtained following *ISO 527-1 (2012)* using three specimens at a loading rate of 10 mm/min (mean strain rate 0.46%/s`). The Young's modulus was determined as the secant modulus between
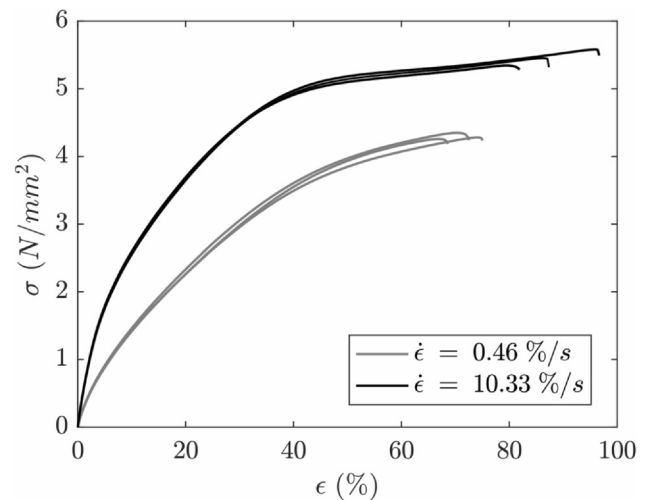

Fig. 1. Stress–strain relations of the visco-elasto-plastic adhesive, for two loading conditions.

0.5% and 5% of the tensile strength, and was found to be 16.0 N/mm^2. The tensile strength and elongation at rupture were determined as 4.3 N/mm^2 and 72.1%, respectively. With a loading rate of 200 mm/ min (mean strain rate 10.33%/s), the values for the Young's modulus, tensile strength and elongation at rupture were determined to be 33.9 N/mm^2, 5.5 N/mm^2 and 88.6% respectively. The significant increase in these values, especially for the Young's modulus, shows that strain-rate dependency plays an important role in the mechanical behavior of the visco-elasto-plastic adhesive. The stress–strain relations of the flexible adhesive are provided in Fig. 1. The material properties for the visco-elasto-plastic adhesive under shear (mode II loading, obtained from the supplier) were quantified using thick adherend shear tests (TAST), partly following *ISO 11003-2:1999* [14]. Aluminum tabs were used, with dimensions of 70 mm $\times$ 25 mm $\times$ 12 mm, as illustrated in Fig. 2. The nominal bondline thickness was 1.75 mm. The test was performed with a constant crosshead rate of 10 mm/min. The shear stress–strain curves are shown in Fig. 3. Similar to the tensile behavior, the loading rate will have a significant influence on the shear stress versus strain relationship.

The reinforced mortar used for the mortar matrix was a polymer-modified mortar containing organic binders, polymer fibres and selected aggregates with a maximum grain size of 1.8 mm. For the preparation of the reinforced mortar, a plastic bonding agent was used in order to improve the adhesion of the mortar matrix to the clay brick substrate, by mixing 110 g of the plastic bonding agent per 10 kg of prepared mortar. The reinforced mortar was prepared following the manufacturer's instructions by adding 2.6 L of water to a bag of 25 kg dry mortar. Both the flexural tensile strength and the compressive strength of the reinforced mortar specimens were determined according to *EN 1015-11* [7]. The mean flexural tensile strength of the reinforced mortar specimens was 7.58 N/mm^2. The compressive strength of the reinforced mortar was 62.6 N/mm^2. The weight density was 2138 kg/ m^3.

The mechanical properties of the materials used for reinforcement are summarized in Table 2.

Table 1
Mechanical properties of the masonry materials used for building the specimens.(Number of tested specimens, n; Coefficient of variance, CoV, provided if n > 3).

	ρ (kg/m^3)	E (N/mm^2)	f_c (N/mm^2)	f_{fl} (N/mm^2)	f_{st} (N/mm^2)
Clay brick	1738	–	31.7[I] (12; 7.4%)	5.89[II] (9; 7.4%)	3.34[III] (12; 8.7%)
Mortar	1745	–	10.6[IV] (16; 20.7%)	3.6[IV] (8; 16.5%)	–
Masonry	–	3100[V] (3)	14.8 (3)	–	–

(I) *EN 772-1* [9]; (II) *ASTM C67-03* [2], (III) A*STM C1006-07* [3], (VI) *EN 1015-11* [8]; (V) *EN 1052-1* (CEN, 2007).
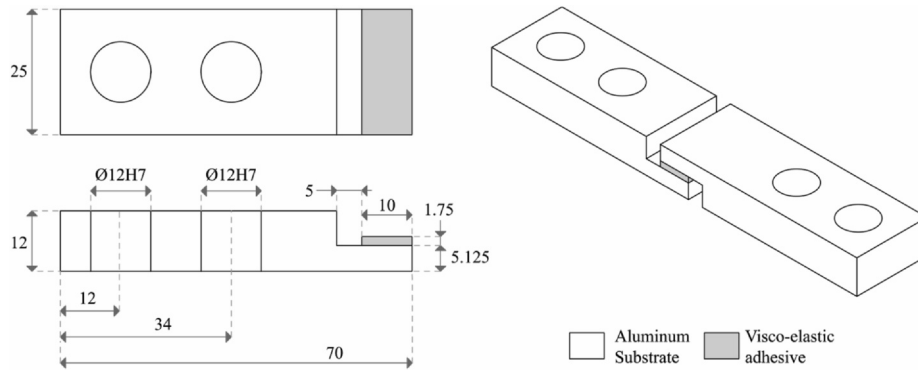
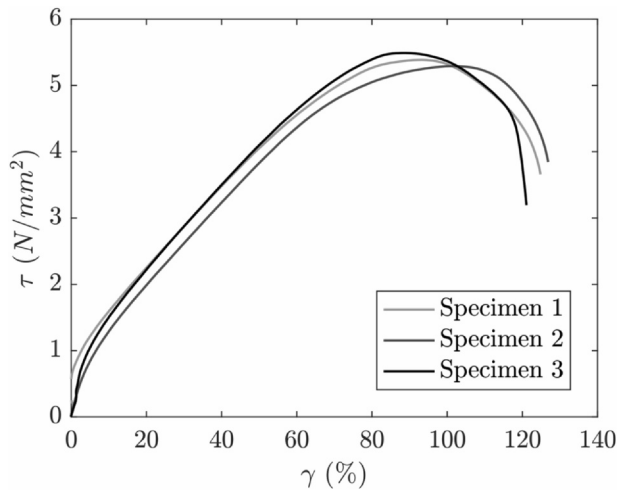**Fig. 2.** Aluminum substrates used for thick adherend shear test.

Fig. 3. Shear stress–shear strain relations of the visco-elasto-plastic adhesive.

Table 2

Mechanical properties of the reinforcement materials. (Number of tested specimens, n; Coefficient of variance, CoV, provided if n > 3).

		Flexible adhesive	CFRP strip	Mortar for cementitious matrix
ρ	kg/m³	1550	1700	2138 (6; 1.7%)
E	N/mm²	16.0 [I] (3)	215,000[IV] (5; 1.0%)	≥25,000
		33.9 [II] (3)		
f_t	N/mm²	4.3 [I] (3)	2876 [IV] (5; 3.4%)	–
		5.5 [II] (3)	–	–
f_{fl}	N/mm²	–	–	7.58 [V] (9; 11.7%)
ϵ_{ult}	%	72.2 [I] (3)	1.59 [IV] (5; 14.7%)	–
		88.6 [II] (3)		
G	N/mm²	20.2 [III] (3)	–	–
τ_{max}	N/mm²	5.4 [III] (3)	–	–
γ_{ult}	%	125.5 [III] (3)	–	–
ν	—	0.48 [I] (3)	–	–
f_c	N/mm²	–	–	62.55[V] (12; 1.6%)

(I) ISO 527-1 [15]: 10 mm/min; $\dot{\varepsilon} = 0.46\%/s$, (II) ISO 527-1 [15]: 200 mm/min; $\dot{\varepsilon} = 10.33\%/s$, (III) ISO 11003-2 [14] modified; (VI) ISO 527-1 [15]: 2 mm/min; $\dot{\varepsilon} = 0.45/min$, (V) EN 1015-11 [8].

2.2. Constructing and reinforcing the pull-out specimens

The prisms were constructed against a vertical sideboard to ensure minimum vertical deviation and were left to cure for 28 days in an unheated environment. The masonry prisms consisted of 6 (number of samples, $n = 3$), 9 ($n = 3$), 12 ($n = 3$) or 16 ($n = 5$) stacked bricks in height(n_b)and had typical mortar joint thicknesses of 13 mm. Each

prism was denoted with the following notation:

$$\overset{v_{machine}}{\underset{n_b}{\underset{\uparrow}{\text{PO-6-100-2}}}} \leftarrow \#$$
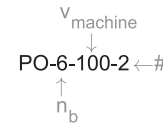
For example, PO-6-100-2 denotes the second prism in the group of 6 stacked bricks that was tested with a machine displacement speed ($v_{machine}$) of 100 mm/min.

After the prisms were sufficiently cured, the retrofitting process of the specimens started by cutting vertical grooves of 65 mm deep and 10 mm wide at the center of the specimens (first step in Fig. 4) by using a cutting machine. The geometric properties of the groove and CFRP strip are provided in Fig. 5. The dust in the groove was removed with compressed air. After cutting to a specified length, but before installation, 20×1.4 mm² ($b_p \times t_p$) CFRP strips were cleaned by wiping with a cloth. Due to a communication error the strips were not cleaned with acetone, as was specified by the supplier of the CFRP strips. Strain gauges (type PFL-10-11, foil strain gauges having polyester resin backing) were attached to alternating sides (to minimize asymmetry effects) of the strip with a constant inter distance of approximately 275 mm for the imbedded strain gauges (SG-1–SG-5), starting from the center of the second brick from the loaded end. The strain gauges that were not imbedded (SG-0) were placed on the loaded end of the CFRP strip, with a distance of 30 mm from the masonry. The strain gauges were covered with wax to reduce the influence of the adhesive on the measurements. The locations of all strain gauges are provided in Fig. 5.

A layer of primer was then applied to the groove to improve the bond between the adhesive and the masonry. After partially filling the groove with the flexible adhesive (step 2 in Fig. 4), the CFRP strip was inserted into the groove using a positioning fork (step 3 in Fig. 4). Excess adhesive to a depth of 30 mm in the grooves was removed using a scraper (step 4 in Fig. 4). After the placement of the strips, the adhesive was left to cure for one day in an unheated environment. The remaining unfilled parts of the groove was filled with reinforcement mortar (final step in Fig. 4). The addition of the reinforcement mortar was done with the purpose of partially restoring the compressive and shear capacity in the groove in order to prevent possible vertical shear failure. The masonry surface was wetted prior to the mortar application to prevent shrinkage. The specimens were left to cure for an additional 28 days in an unheated environment. A schematic overview of the reinforced specimens is provided in Fig. 5.

It should be noted that the bond-stacked masonry assembly used in the current study is not representative of traditional, running bond masonry. However, no significant deviations in the obtained CFRP strip bond behavior are expected when the vertical grooves do not coincide with the head joints of the running bond masonry in real life applications.
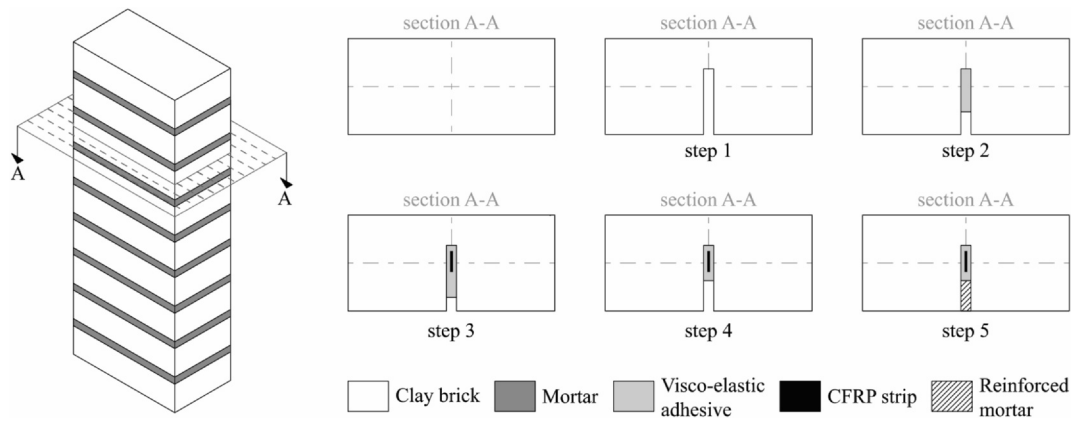
Fig. 4. Schematization of the reinforcement process using the cross-sectional view of the specimen along the height.

2.3. Test setup and procedure

As there are as-yet no standardized guidelines for performing pull-tests, the experiments were performed following the recommendations of [27]. The direct pull-out tests were conducted on an Instron universal testing machine, see Fig. 6. An illustration of the setup is provided in Fig. 7. Before the experiment, aluminum plates of 110 mm in length,

20 mm in width and 2 mm in thickness were tapered at an angle of 12°, following the tabbing guide for composite test specimens [1]. After the tabs were roughened with sandpaper and thoroughly cleaned with acetone, the tabs were glued to both sides of the CFRP strip at the loaded end using high strength and fast-curing epoxy (see Fig. 7).

The process continued by carefully positioning the prism under the loading grips of the testing equipment, with the specimen resting on
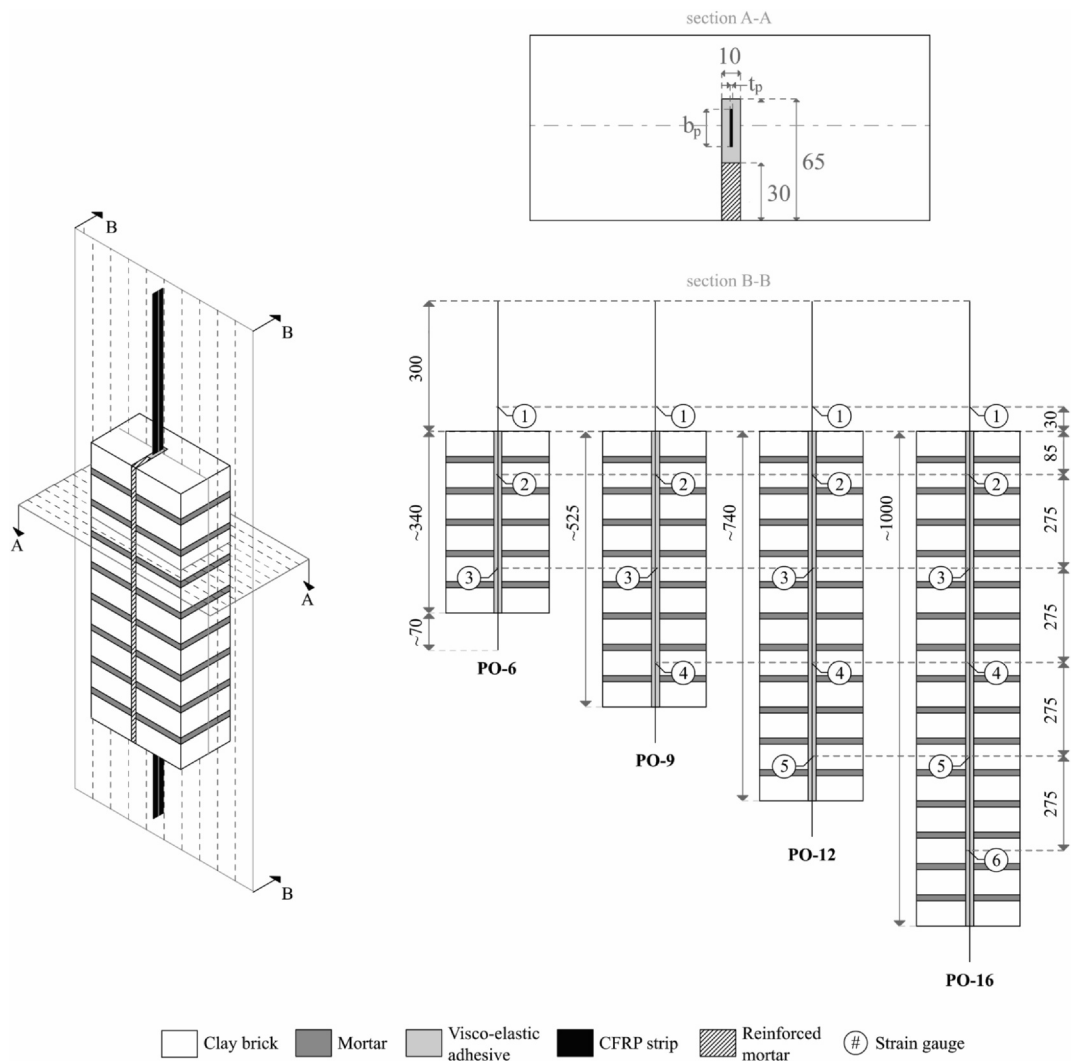

Fig. 5. Schematic overview of the different specimen geometries and location of sensors.

Fig. 6. Photo of the test setup.

two support blocks. Hard cardboard was put on the top of the prism to prevent stress concentrations due to a possible non-flat surface of the brick. A steel restraint plate was placed on top of the prism at the loaded end (Fig. 8). To prevent undesirable wedge type failure modes, the plate was 25 mm thick and provided full bearing against the specimen, with the exception of three small openings: one for the CFRP strip and two for LVDTs. The specimen was then lifted up via the tapered aluminum grip plates. This procedure made it possible for the
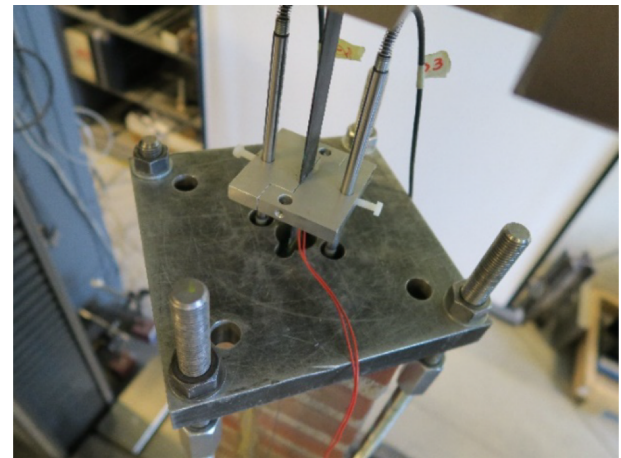
Fig. 8. Restraint plate and loaded-end instrumentation.

prism to settle into a balance condition and thus minimize the eccentricity caused by possible imperfect installation of the CFRP strips. Using M12 threaded steel rods, the steel restraint plate was bolted to the base of the installation until a pre-loading force of 1.6 kN was monitored (1.0 kN for the PO-6 and PO-9 specimens) at the loading grips of the testing equipment. The pre-loading was done with the purpose of letting the prism continue to settle into a balance condition. It should be noted that the pre-tensioning of the CFRP strip is not a common feature in real applications of the FDM CFRP retrofit system.

Prior to the load application process, eight LVDT sensors were installed (6 for the PO-6 and PO-9 specimens). The upper two 20 mm range sensors measured the loaded-end slip and the bottom two 20 mm range sensors measured the free-end slip. The mean of the two LVDTs was used to establish the corresponding slip. Prior to the analysis, the loaded-end slip was corrected for the elongation of 70 mm of CFRP strip outside the specimen. In order to measure the axial deformation within the masonry, additional short range LVDT sensors were applied: four to the PO-16 and PO-12 specimens, and two to the PO-9 and PO-6 specimens. After resetting the sensors, the experiment was started with the pre-determined pull-out speed. Due to errors, the data from the sensors for the first two specimens tested (PO-16-5 and PO-16-25) were logged with only 2.5 Hz, giving limited data-points. The remaining specimens
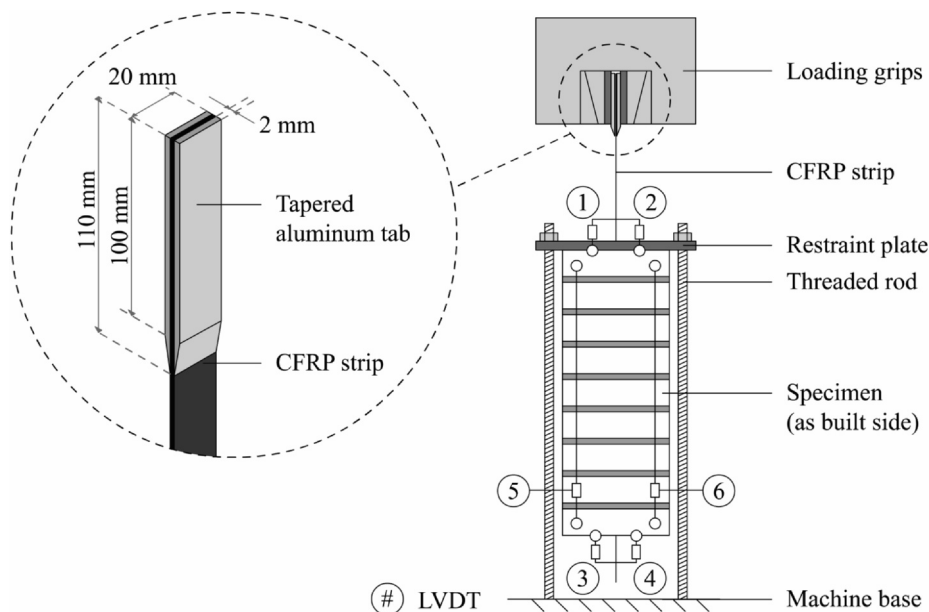

Fig. 7. Schematic overview of the test setup.

had an increased logging frequency of 20 Hz.

2.4. Processing the strain-gauge readings

In order to establish the shear stress versus slip behavior using the embedded strain gauges, a one-dimensional partial-interaction (PI) model was used as illustrated in Fig. 9. It should be noted that due to symmetry, only half of the specimen is depicted. For the partial-interaction model only the shear component was included. It was assumed that no significant tensile stresses would develop at the interface between CFRP strip and adhesive with the considered loading scheme. It should be noted that when a one-way spanning retrofitted wall is subjected to out-of-plane loading, tensile stresses at the interface between the CFRP and the adhesive can conceivably develop.

Based on the active strain gauges, a second-order polynomial was constructed for the strain distribution over the entire embedded length at each instant of measurement, using the boundary condition of zero strain in the CFRP strip at the free end($\varepsilon_0 = 0$). The model was based on dividing the specimen into elements of 1 mm length. For each element, the decrease in tensile force in the CFRP strip was approximated using the constructed polynomial and Eq. (1), where$\varepsilon_{p,i}$ is the strain of the CFRP strip at position 'i' and E_P is the Young's modulus of the CFRP.

$$\Delta F_i = (\varepsilon_{p,i} - \varepsilon_{p,i-1}) \cdot E_P \cdot b_p \cdot t_p \tag{1}$$

The decrease in tensile force is in equilibrium with the sum of the bond stress over the length and perimeter of the element, as provided in Eq. (2). Combining Eqs. (1) and (2), and making the assumption that the CFRP thickness is negligible compared to the width($b_p + t_p \approx b_p$), results in Eq. (3). At each node, the local slip of the CFRP was calculated using the slip at the previous node and the average FRP strain over the element, as per Eq. (4).

$$\Delta F_i = \tau_i \cdot \Delta x \cdot (2b_p + 2t_p) \tag{2}$$

$$\tau_i = \frac{(\varepsilon_{p,i} - \varepsilon_{p,i-1}) \cdot E_P \cdot t_p}{2 \cdot \Delta x} \tag{3}$$

$$\delta_i = \delta_{i-1} + \frac{(\varepsilon_{p,i} - \varepsilon_{p,i-1})}{2} \cdot \Delta x \tag{4}$$

3. Test results and discussion

The test results are summarized in Table 3. A generalized representation of the force-slip behavior is shown in Fig. 10, along with five derived parameters: the initial stiffness(k_{ini}), pull-out strength(P_{max}), the corresponding slip at the loaded end($\delta_{L,max}$), the pull-out force at the end of the test(F_{end}), and the corresponding slip at the loaded end at the end of the test($\delta_{L,end}$). The initial stiffness (k_{ini}) was determined as the secant modulus at 35% of the pull-out strength(P_{max}). The force F_{end} represents the (residual) force at the final moment of measurement where all LVDTs measuring the slip were gathering data.

The initial loaded-end slip rate of the CFRP strip($\dot{\delta}_{L,ini}$), the Young's modulus of the CFRP strip (E_P), the maximum deformation of the masonry over the length(Δ_{mas}), the governing failure mechanism and the damage to the masonry substrate are also provided in Table 3. All mentioned parameters will be covered in the following sections.

3.1. Failure mechanisms and damage to masonry

In all specimens, except PO-16-25, PO-16-100-1 and PO-16-100-2, splitting of the masonry prism was observed. A typical crack is shown in Fig. 11. The general observation was that the crack initiation occurred near the loaded end when the pull-out strength was reached, and propagated over the entire bonded length during the post-peak phase. Despite splitting, specimens did not fall apart due to small regions of intact flexible adhesive. The splitting was an unavoidable aspect of the selected test method. The pull-out experiments were conducted in the absence of lateral confinement pressure, which may exist in the practical situations. When the confinement is significant, gradual changes from splitting to a pull-out failure can be observed [23].

Based on observation of the loaded end, the predominant failure mechanism was determined as cohesive failure in the adhesive. After breaking the specimens in two using a chisel and a hammer, the previously observed cohesive failure mechanism was confirmed with the exposed embedded CFRP strip. A typical photo of an embedded CFRP strip after breaking the specimen is shown in Fig. 12.

For specimens PO-16-25, PO-16-100-1 and PO-16-100-2, which failed due to CFRP rupture, no splitting of the masonry was observed. Fig. 13a shows the undamaged treated side of the considered specimens. On the as-built side, hairline cracks were observed along the 6 bricks at the loaded end (Fig. 13b). Local crushing failure at the loaded end was also observed, as shown in Fig. 14.

3.2. Global force-slip behavior

The global force-slip diagrams for the tested specimens, taking into account both the free end (dashed lines) and the loaded end (solid lines), are shown Fig. 15. It should be noted that for improved plot representation, the loaded-end slip is presented with an initial offset of 10 mm. CFRP rupture in Fig. 15 is marked with an 'x'.

An overarching observation is that the global force-slip relations remain consistent within the same specimen group. The highest deviation is observed in the specimen pull-out strength, which can be attributed to the imperfect placement of the CFRP strips. Looking at the initial stiffness, an increasing trend is observed with longer embedment lengths, as shown in Fig. 16. The initial stiffness ranged from 8.8 kN/mm (PO-6-100-1) to 14.6 kN/mm (PO-16-100-1). A strong linear correlation ($R^2 = 0.70$) was found between the initial stiffness and the embedment length.

A very strong linear correlation was found between pull-out strength and the embedment length range of the performed tests, as
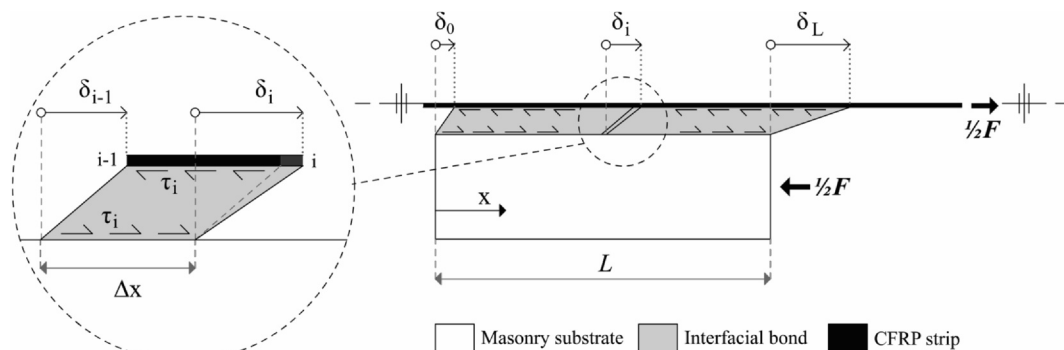

Fig. 9. One-dimensional partial- interaction (PI) model. Due to symmetry, half of the specimen is depicted.

Table 3
Overview pull-out test results.

Specimen	L (mm)	$\dot{\delta}_{L,ini}$ (mm/s)	E_P (N/mm^2)	k_{ini} (kN/mm)	P_{max} (kN)	$\delta_{L,max}$ (mm)	F_{end} (kN)	$\delta_{L,end}$ (mm)	Δ_{mas} (mm)	Governing failure mechanism	Damage to masonry
PO-6-100-1	340	0.92	197,000	10.4	38.7	5.9	6.9	18.3	0.05	(A)	(1)
PO-6-100-2	342	1.12	201,000	8.8	33.1	4.3	6.4	18.6	0.05	(A)	(1)
PO-6-100-3	347	1.03	194,000	10.0	33.5	4.1	5.7	18.9	0.08	(A)	(1)
PO-9-100-1	524	1.09	200,000	9.1	42.6	6.0	8.2	18.1	0.28	(A)	(1)
PO-9-100-2	525	1.01	204,000	11.0	53.3	6.9	6.6	18.6	0.12	(A)	(1)
PO-9-100-3	529	1.03	200,000	11.2	39.5	5.5	8.7	17.0	0.07	(A)	(1)
PO-12-100-1	729	1.07	204,000	11.8	63.6	7.4	8.2	18.1	0.15	(A)	(1)
PO-12-100-2	735	1.04	203,000	10.9	54.3	7.6	19.4	13.3	0.23	(A)	(1)
PO-12-100-3	732	1.10	202,000	10.4	52.8	6.1	6.5	16.9	0.17	(A)	(1)
PO-16-5	1001	0.04	199,000	13.3	68.0	8.6	13.7	18.2	0.66	(A)	(1)
PO-16-25	998	0.22	204,000	11.5	81.0	9.7	81.0	9.7	0.44	(B)	(2)
PO-16-100-1	996	0.93	203,000	14.6	87.8	7.9	87.8	7.9	0.19	(B)	(2)
PO-16-100-2	995	1.04	220,000	12.2	83.2	8.6	83.2	8.6	0.25	(B)	(2)
PO-16-100-3	992	1.00	214,000	13.8	80.1	12.0	22.3	19.0	0.46	(A)	(1)

(A) Cohesive failure adhesive; (B) Rupture CFRP; (1) Clear cracks, both sides, entire length; (2) Hairline cracks top six bricks of untreated side.
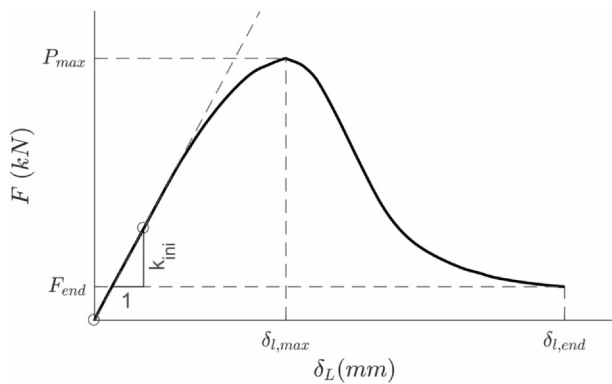

Fig. 10. Global force - (loaded-end) slip behavior.

Fig. 12. Close-up of the embedded CFRP strip of specimen PO-12-100-2 after the test, showing the predominant cohesive failure.
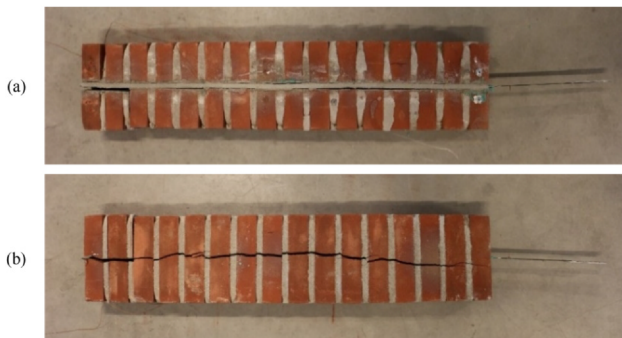

Fig. 11. Photos of the treated side (a) and as-built side (b) of specimen PO-16-100-3.

Fig. 13. The undamaged treated side (a) and cracked (top 6 bricks) as-built side (b) of specimen PO-16-100-4.

shown in Fig. 17. This linear dependency was also observed for similar test configurations with short bonded lengths [4,27]. The linear relation between pull-out strength and the embedment length within the current experimental campaign was found to be applicable until the load capacity became sufficiently large that rupture of the CFRP started to govern. The pull-out strength was 82.8 kN, meaning that an embedment length of ~1 m was sufficient to initiate CFRP rupture($T_P = 80.5$ kN) governed failure mechanism instead of cohesive failure. It should be noted that in the context of partial-interaction mechanics, a linear dependency between P_{max} and L occurs only for short bond lengths while the shear stress distribution along the bonded length remains near-uniform. The agreement between the observed trend and a PI model is further demonstrated in Section 5. Looking at the effect of the initial loaded-end slip rate ($\dot{\delta}_{L,ini}$) on the pull-out strength, a strong logarithmic
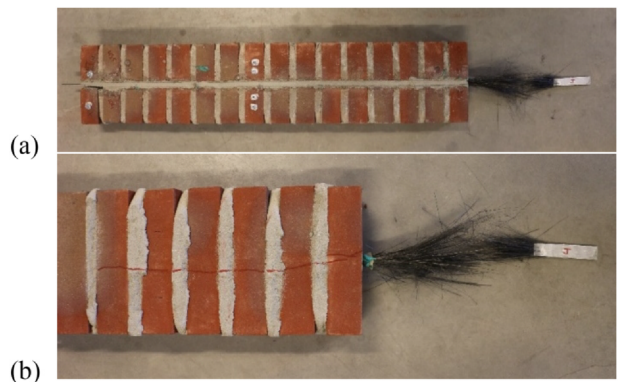
correlation was found, as shown in Fig. 18. The initial loaded-end slip rate was determined as the mean loaded-end slip rate from the start of the pull-out experiment up to and including the moment where 35% of the pull-out strength was reached. The pull-out strength corresponding to $\dot{\delta}_{L,ini} \approx 0.004$ mm/s (0.5 mm/min machine displacement speed) was taken from a previous experimental campaign [25]. It was observed that while keeping the embedment length constant at ~1 m, increasing the machine speed from 0.5 mm/min to 100 mm/min ($\dot{\delta}_{L,ini} \approx 1.0$ mm/s) led to a 67% increase in pull-out strength, with the governing failure mechanism shifting from cohesive failure to CFRP rupture. Looking at the PO-16-5, PO-16-25 and PO-16-100 specimens,

Fig. 14. Close-up of the loaded end of specimen PO-16-100-4, showing the governing failure mechanism: CFRP rupture.

the pull-out speed had no significant effect on the initial stiffness.

3.3. Local bond-slip behavior

The process of obtaining the local bond-slip behavior using the embedded strain gauge readings is demonstrated using specimen PO-12-100-1. Based on the active strain gauges and the boundary condition at the free end (no strain), a second-order polynomial was constructed for the strain value over the entire embedded length for each instant of measurement. These polynomials for different pull-out loads are shown in Fig. 19a and b for the pre-peak and post-peak phase respectively. The determined polynomial was rejected if either the number of active and embedded strain gauges reduced to one, or the polynomial showed an upward slope at the free end. The latter rejection case is shown with a thick solid line in Fig. 19b.
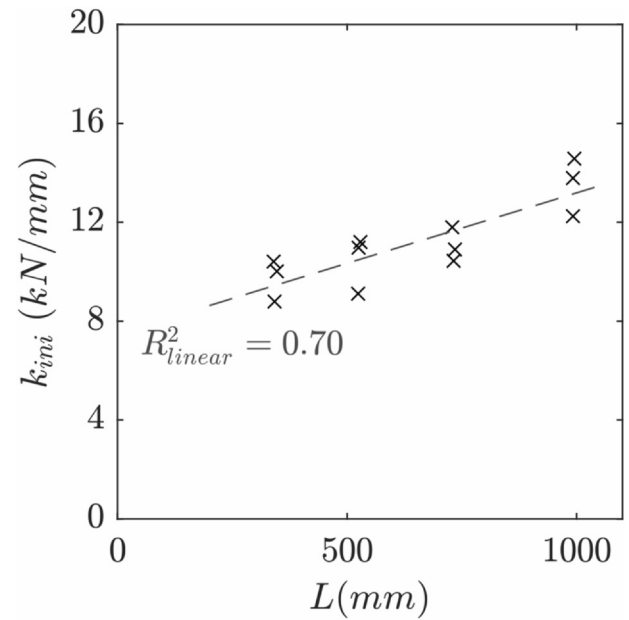
Fig. 16. The initial stiffness k_{ini} as a function of the embedded length L for specimens tested at $v_{machine} = 100$ mm/min.

Looking at the PO-xx-100 specimens, it was observed that the free-end bond-slip behavior showed a steep increase. This phenomenon of a stiffer local bond-slip response was also observed with the PO-16-5 and PO-16-25 specimens, as shown in Fig. 21. Due to damaged sensors and/or failure of the specimen, the full local bond-slip behavior at the free end could not be determined. With specimen PO-0.5-16 from the previous work of the authors [25] more insight was obtained.

From Fig. 21 it was observed that the steeper increase in local bond-slip behaviour at the free end continued until a significantly higher local bond strength (with respect to the loaded end) was reached. This
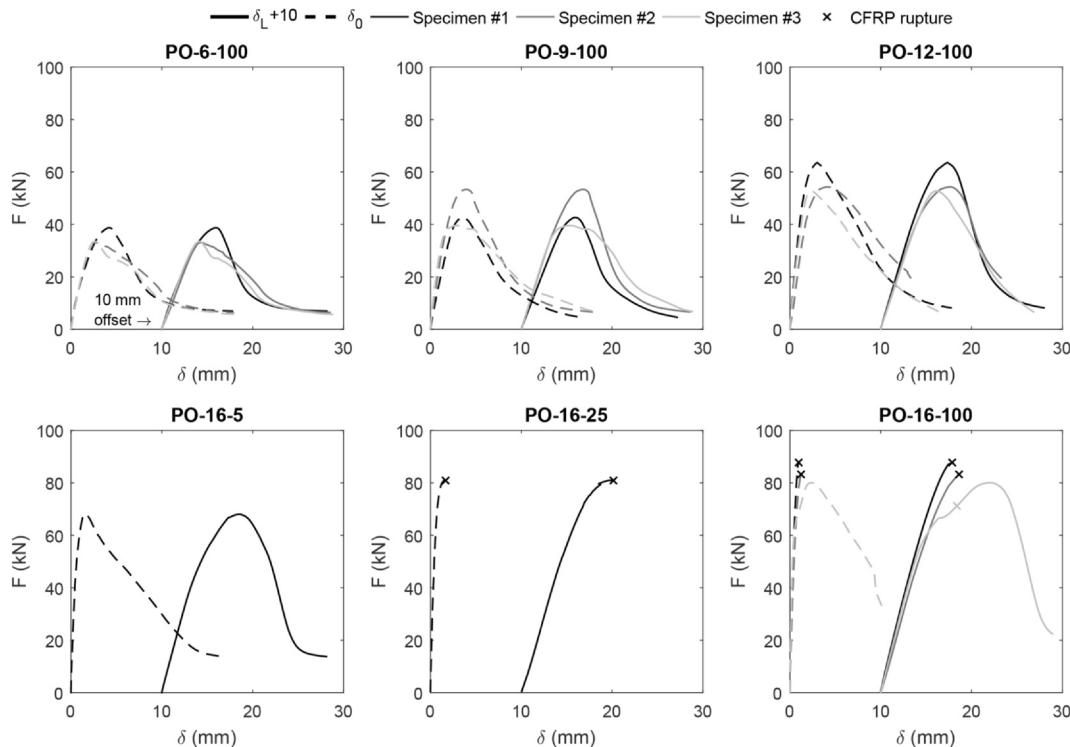

Fig. 15. Loaded-end and free-end slip plotted against the force. The loaded-end slip is presented with an initial offset of 10 mm solely for improving the plot representation.
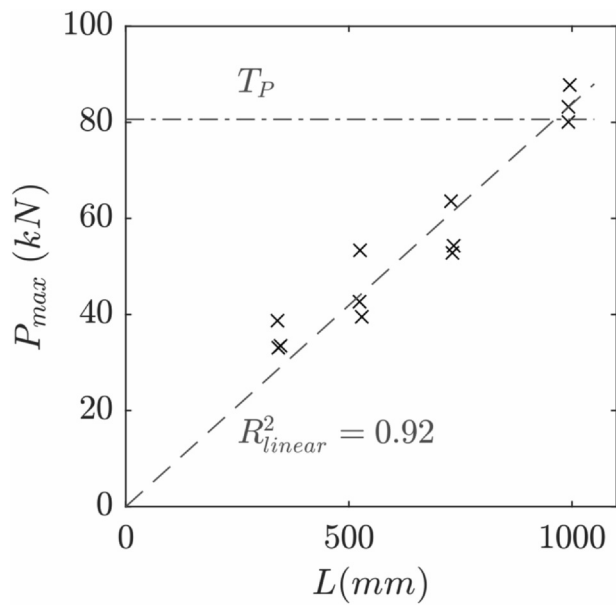
Fig. 17. The pull-out strength P_{max} as a function of the embedded length L for specimens tested at $v_{machine}$=100 mm/min.
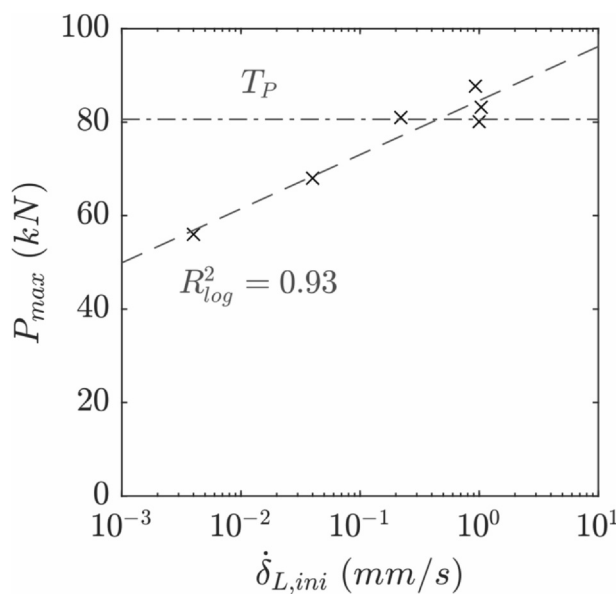

Fig. 18. The pull-out strength P_{max} as a function of the initial loaded-end slip rate $\dot{\delta}_{L,ini}$ for specimens with an embedment length of 1 m.

phenomenon of a stiffer and stronger local bond-slip response can be attributed to the visco-elasto-plastic properties of the adhesive and the non-uniform pull-out speed. Fig. 22 provides the local bond strength (τ_{max}) and corresponding slip rate at the loaded end ($\dot{\delta}_L$), free end, and strain gauge locations for the PO-6-100, PO-9-100 and PO-12-100 specimens. For the PO-6-100-1 and PO-6-100-3 specimens, the local bond strength seems to remain constant over the embedment length. With the PO-9-100 and PO-12-100 specimens, the local bond strength reduces from the loaded end towards the mid-embedment length. This finding agrees with fracture mechanics theory in that the propagation of cracks occurs at stresses lower than the critical stress required for fracture. However, somewhat unexpectedly, the local bond strength increased from the mid embedment length towards the free end for the PO-9-100 and PO-12-100 specimens, as illustrated in Fig. 22.This increase is linked to the increase of the corresponding slip rate. Despite the machine displacement rate being constant, the finite stiffness of the

machine, the threaded rods (used to connect the restraint plate to the base of the machine) and the CFRP strip between the masonry and the grips of the machine disrupted the loaded-end slip rate. The elongation rate of the machine, the threaded rods and the free CFRP strip at the loaded end resulted in a decrease of the actual slip rate at the loaded end. The mean slip-rate at the loaded end was ~70% of the machine displacement speed for all the specimens. This was applicable as long as there was an increase in exerted pull-out force. During the post-peak phase, where the applied pull-out force started to decrease, the relaxation rate of the aforementioned (finite stiffness) components resulted in an increase of the actual slip rates. This increase in local slip rate, being more significant for longer specimens, resulted in higher local bond strength due to the strain-rate dependent properties of the visco-elasto-plastic adhesive.

The contour plots of the local bond development over the embedded length, as a function of the loaded-end slip, is provided in Fig. 23. The load is represented with the solid black curve (secondary y-axis). It should be noted that the full range of the contour plots could not be given due to the limited strain gauge readings.

In all cases, the maximum pull-out load was reached in the phase where the maximum local bond stresses shifted from the loaded end ($x = L$) towards the free end ($x = 0$). Specifically, when the local τ-δ correlation at the loaded end passed the post-peak stage and the local τ-δ correlation at the free end neared its peak, the specimen reached full strength. It should be noted that this shift of stresses happened rapidly. Furthermore it was observed that with increasing bond length, there was a clear distinction between the level of bond stresses near the loaded end and free-end region on one side, and the level of bond stresses at mid-embedment length on the other side.

4. Tri-linearization

With the obtained local bond-slip correlations, as was shown in Fig. 20, a general local bond-slip relation can be determined for modelling purposes. The first step to reach a general local bond-slip correlation is to construct an averaged local bond-slip relation for the PO-6-100, PO-9-100 and PO-12-100 specimens. The PO-16-100 specimens were not considered due to the incomplete bond-slip relations. The averaged curve is shown with a solid grey line in Fig. 24 for specimen PO-6-100-1. This averaging process, based on slip increments of 0.4 mm, continued while three or more local bond-slip relations were present. The end point of the averaged curve is denoted with δ_a and τ_a. The bond energy under the averaged curve is determined using Eq. (5):

$$G_f = \int \tau_{averaged}(\delta)d\delta \tag{5}$$

The second step to reach an averaged local bond-slip correlation is to multi-linearize the averaged local bond-slip curve of the considered specimens. The multi-linearized local τ-δ behavior at the CFRP-adhesive interface consists of four zones: elastic (I), damage initiation (II), damage development (III), and residual (IV), as shown in Fig. 25. This is a modification of the bi-linear frictional rule as reported by Vaculik et al. [28]. The local τ-δ at the interface can be expressed with the set of conditional equations as provided in Eqs. (6a)–(6d), where $k_1 = (\tau_f/\delta_1)$ and $k_2 = (\tau_f - \tau_r)/(\delta_3 - \delta_2)$.

$$\tau_{ml}(\delta)\begin{cases} k_1\tau_f \\ \tau_f \\ \tau_f - k_2(\delta - \delta_2) \\ \tau_r \end{cases} \delta \leq \delta_1 \tag{6a}$$

$$\delta_1 < \delta \leq \delta_2 \tag{6b}$$

$$\delta_2 < \delta \leq \delta_3 \tag{6c}$$

$$\delta > \delta_3 \tag{6d}$$

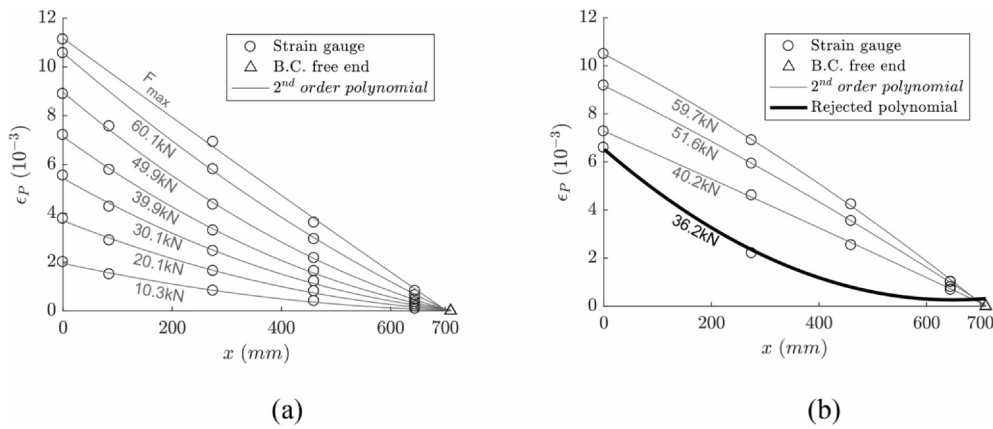The value for the damage initiation plateau, τ_f, was determined in

Fig. 19. Obtained second order polynomials of the strain distribution along the embedded length, using the strain gauge readings for specimen PO-12-100-1: pre-peak (a) and post-peak phase (b).

accordance with Eq. (7).

$$\tau_f = 0.95\tau_{max} \tag{7}$$

The initial stiffness is determined as a secant modulus at 35% of the bond strength. Using the initial stiffness and the value for the damage initiation plateau τ_f, the value for δ_1 can be determined. As the bond

energy for the multi-linearized and averaged bond-slip relation until slip δ_a are assumed equal, the value for δ_2 can be determined following Eq. (8). This way the bond energy is determinative of the final shape of the multi-linearized bond-slip relation.

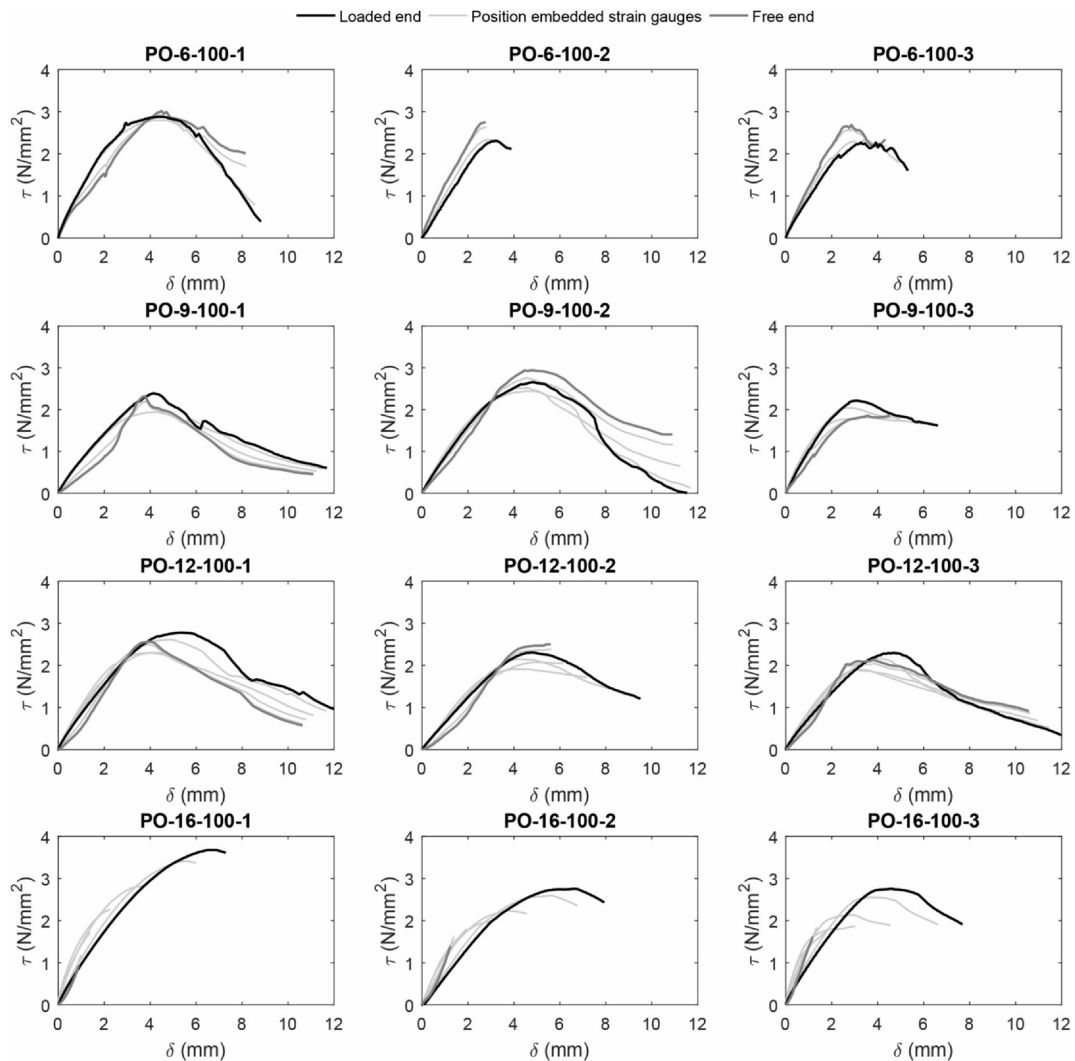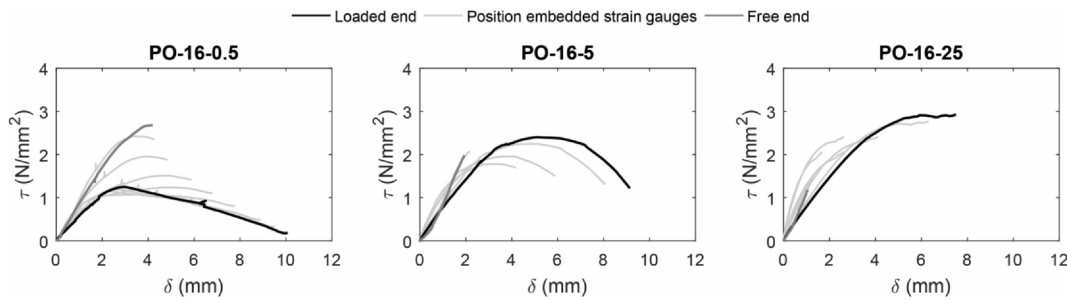**Fig. 20.** Local bond-slip relations of the specimens tested with $v_{machine} = 100$ mm/min.

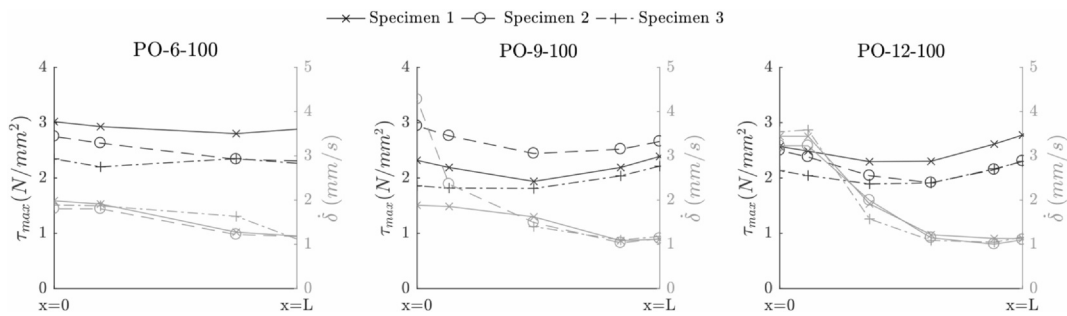**Fig. 21.** Local bond-slip relations PO-16-15 [25], PO-16-5 and PO-16-25 specimen.

Fig. 22. Local bond strength (τ_{max}) and corresponding slip rate ($\dot{\delta}$) at the loaded end, free end and strain gauge locations.

$$\delta_2 = \frac{2G_f - (\tau_f + \tau_a)\delta_a + \tau_f\delta_1}{\tau_f - \tau_a} \tag{8}$$

Using δ_a, τ_a, δ_2, τ_f and the residual bond stress τ_r (estimated at 0.4 N/mm^2 based on the measured forces at the end of the tests), the value for δ_3 can be determined by means of linear extrapolation.

The multi-linearized τ-δ relations for the PO-6-100, PO-9-100 and PO-12-100 specimens are shown in Fig. 26. By averaging these, a global-average multi-linear τ-δ correlation was determined. It should be noted that the post-peak part of the multi-linearized bond-slip curve could not be determined for specimens PO-6-100-2 and PO-6-100-3 due to incomplete data, so these specimens were excluded from the averaging process. The averaged multi-linear τ-δ relation was found to be a good representation of all the obtained τ-δ relations for the PO-6-100, PO-9-100 and PO-12-100 specimens, as shown in Fig. 27.

The parameters defining the averaged multi-linear τ-δ relation are provided in Table 4. In general, the interfacial fracture energy (G_f) is defined as the area under the τ-δ curve. Vaculik et al. [28] considered this integral only up to the slip at debonding (δ_3) as the integral becomes unbounded for $\tau_r > 0$. Using this definition, the interfacial fracture energy was determined as 16.9 N/mm.

5. Partial-interaction model

The one-dimensional partial-interaction (PI) model, as presented in Section 2.4 and shown in Fig. 9, was used to model the F-δ relation based on the multi-linear local τ-δ relation obtained in Section 4. Rewriting Eq. (3) results in Eq. (9), where the strain is calculated based on the multi-linear τ-δ relation. The shear stress was determined in accordance with Eqs. (6a)–(6d) and the parameters presented in Table 4 regarding the averaged multi-linear local bond-slip behavior.

$$\varepsilon_i = \varepsilon_{i-1} + \frac{2\Delta x \cdot \tau(\delta_{i-1})}{E_p \cdot t_p} \tag{9}$$

The free-end slip δ_0 was used as an input for the model. The strain in the CFRP strip must be zero at the free end ($\varepsilon_0 = 0$). The force transferred from the CFRP strip to the flexible adhesive was determined in accordance with Eq. (1). The local slip of the next element was obtained using Eq. (4). The pull-out load $F(\delta_0)$ and the loaded-end slip $\delta_L(\delta_0)$

were determined using Eqs. (10) and (11) respectively.

$$F(\delta_0) = 2b_p \sum_{i=1}^{L} \tau_i \tag{10}$$

$$\delta_L(\delta_0) = \delta_0 + \sum_{i=1}^{L} \varepsilon_i \tag{11}$$

The F-δ relation was determined for different anchorage lengths, as shown in Fig. 28. The end of the elastic (δ_1), damage initiation (δ_2) and damage development (δ_3) zones from the interfacial constitutive law are highlighted with circles, squares and diamonds respectively. The results following from the proposed model show good agreement with the experimental outcomes. The only exception is for an anchorage length of 1000 mm, where the model seems to result in a significant steeper decrease in the post-peak region (marked with a light grey area). This difference can be attributed to the non-uniform local slipping speeds and the strain-rate dependent properties of the visco-elasto-plastic adhesive.

The contour plots of both the modelled and experimentally determined local bond development over the embedded length, as a function of the loaded-end slip, is provided in Fig. 29. From each specimen group, the specimen with the broadest measured range is selected for the comparison. Comparing the modelled and experimentally determined local bond development over the embedded length, it can be concluded that the model provides a good approximation, especially when looking at the shape of the contour plots. Unlike the experimental results, the model shows no higher shear stresses.

With the partial-interaction model and the input parameters as provided in Table 4, $F - \delta$ relations were determined for various anchorage lengths, ranging from 400 mm to 1800 mm in increments of 100 mm, as shown in Fig. 30. The shear stress distributions at the instance of peak pull-out strength are shown in Fig. 31.

Up to and including an anchorage length of 550 mm, the pull-out strength is reached when the free-end slip is equal to δ_1 (2.82 mm). Over this bonded length range, the peak strength coincides with a near-uniform stress distribution where the entire bonded interface is in the damage initiation phase, and each additional 100 mm of bonded length increases the pull-out strength by around 8.9 kN.
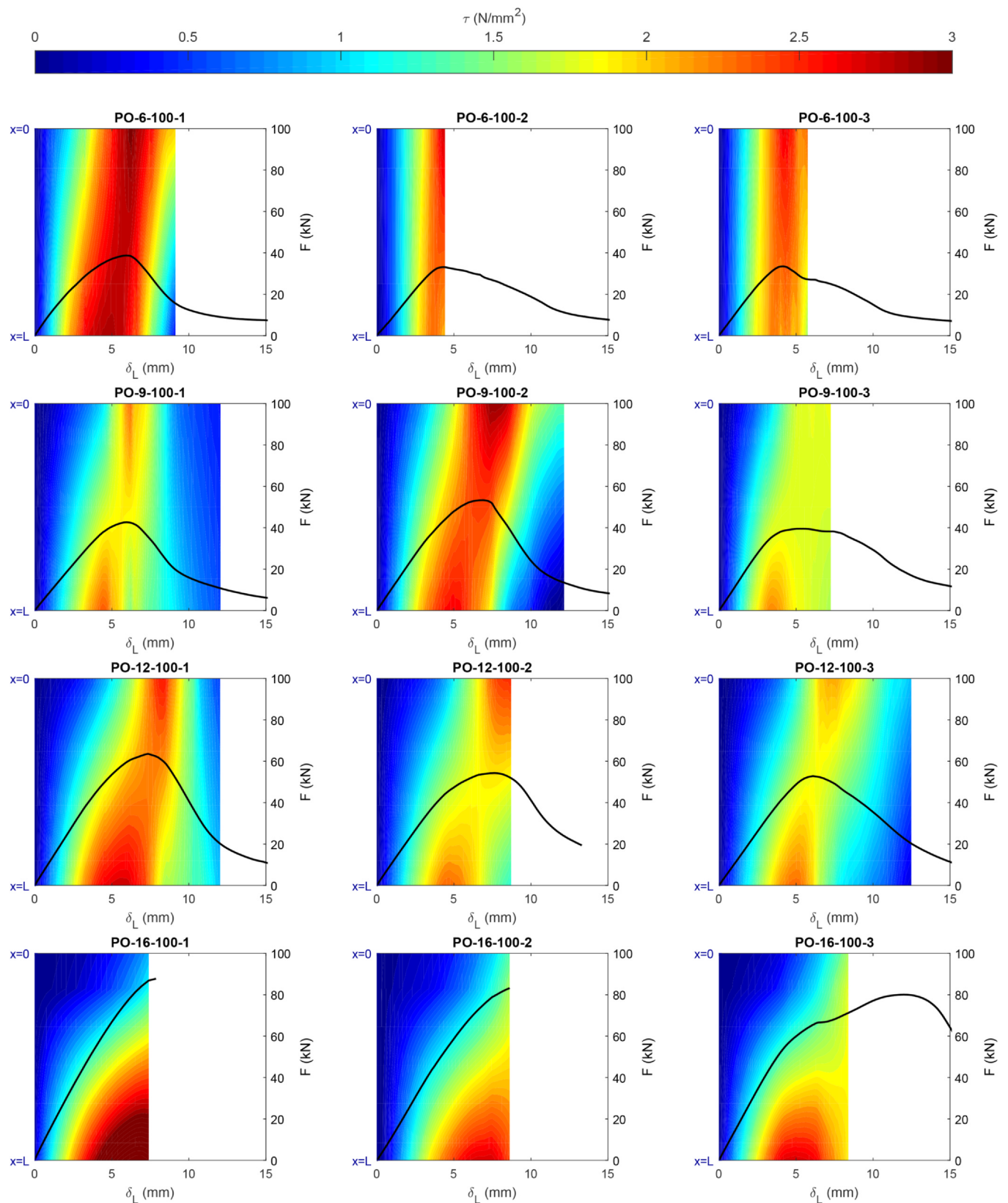
Fig. 23. Contour plots of the local bond development over the embedded length, as a function of the loaded-end slip. Black curves show the pull-out load.

Increasing the bonded length from 550 to 1300 mm, it can be observed that each additional unit of bonded length results in a less effective increase of the pull-out strength. In this analysis the tensile strength of the CFRP strip is not taken into account. The loaded-end slip shifts towards 12 mm (damage development zone) whereas the free-end slip shifts towards 1.7 mm (elastic zone) at the instance when the pull-out strength is reached. The plateau of damage initiation shifts from the free end towards the loaded end, covering a bonded length of 550 mm.
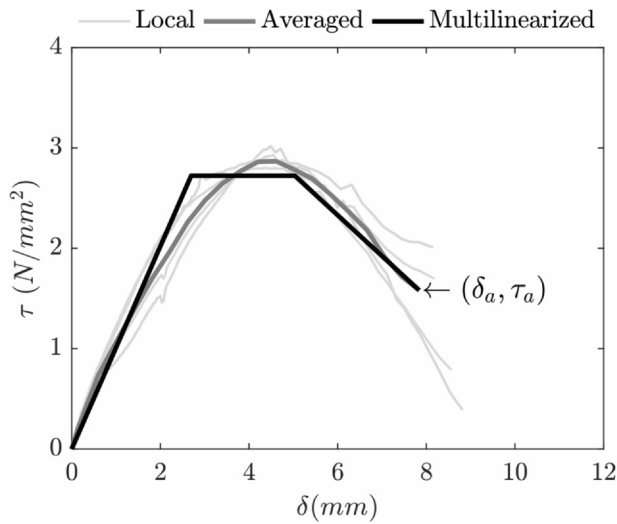
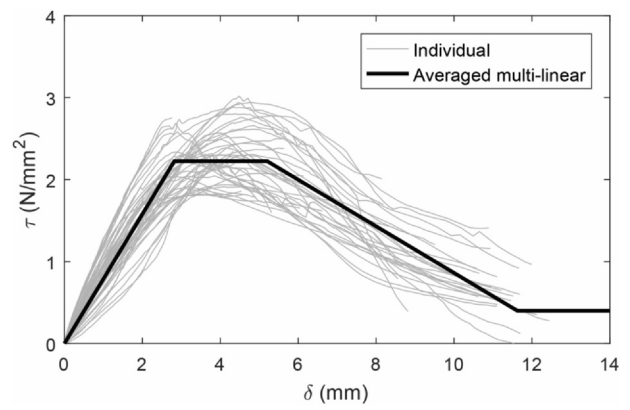Fig. 24. Generalization and multi-linearization of the obtained local bond-slip relations of PO-6-100-1.

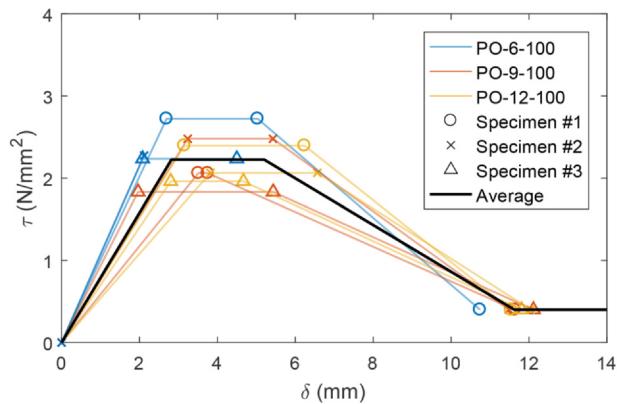Fig. 25. Local τ-δ relation to represent the bond behavior along the bond interface (CFRP-adhesive).

Fig. 26. Multi-linearized τ-δ relations (individual tests and averaged) for the PO-6-100, PO-9-100 and PO-12-100 specimens.

For bonded lengths of 1300 mm or longer, the pull-out strength is reached when the free-end slip equals 1.7 mm. The bonded interface remains in the elastic zone between x = 0 (free end) and x = 120 mm. Between x = 1100 mm and x = 1300 mm, the adhesive interface is in the residual zone, where the shear stress is solely caused by friction.

Fig. 27. Averaged and multi-linearized τ-δ relation and all the obtained τ-δ relations for the PO-6-100, PO-9-100 and PO-12-100 specimens.

Table 4
Parameters averaged multi-linear local bond-slip behavior.

Parameter	Value	Unit
τ_f	2.22	N/mm^2
τ_r	0.40	N/mm^2
δ_1	2.82	mm
δ_2	5.20	mm
δ_3	11.62	mm
G_f	16.87	N/mm

Increasing the bonded length above the critical value (1300 mm) has limited effect on the pull-out strength, because any incremental increase is only due to residual stress, so that every 100 mm of bonded length only increases the pull-out strength by an additional 1.6 kN.

The force versus loaded-end slip relation of the flexible adhesive mounted CFRP strip, following from the partial-interaction analysis, is provided in Fig. 32 for various anchorage lengths. When the loaded end enters the damage development zone ($\delta_L \geq \delta_2$), especially for bonded lengths over 200 mm, the load can still increase. This increase becomes more significant for higher bonded lengths. Entering the damage development zone at the loaded end, the shear stresses for the remaining part of the bonded length can further increase the load since the bond law is still either in the linear elastic zone (towards the free end) or the damage initiation zone. For bonded lengths of 500 mm or less, the load is either in, or very close to the residual phase. This would mean that at the moment the loaded end region enters the residual zone of the local bond law, the pull-out load will enter the residual phase either instantly or very soon. Considering the tensile limit of the CFRP strip, Fig. 32 shows for bonded length of 1250 mm or higher the CFRP rupture (marked with an 'x') starts to govern, according to the partial-interaction analysis. When CFRP rupture is the governing failure mechanism, the residual zone of the local bond law is not entered over the entire bonded length.

The pull-out strength versus the bonded length, predicted using the partial-interaction analysis, is provided in Fig. 33. Over the experimentally tested bonded lengths (L = 340 to 1000 mm), the analysis demonstrates the relationship between P_{max} and L to be almost linear (R^2 = 0.98), in agreement with the experiment. It should be noted that this linear trend is only apparent because of the lengths considered and the fact that the rupture of CFRP caps off the strength at a bonded length of ~1000 mm. If we ignore rupture, then the curve begins tapering off for L beyond ~1000 mm, and once L reaches the critical bond length of ~1300 mm the enhancement in strength is only due to increased residual friction along the interface.
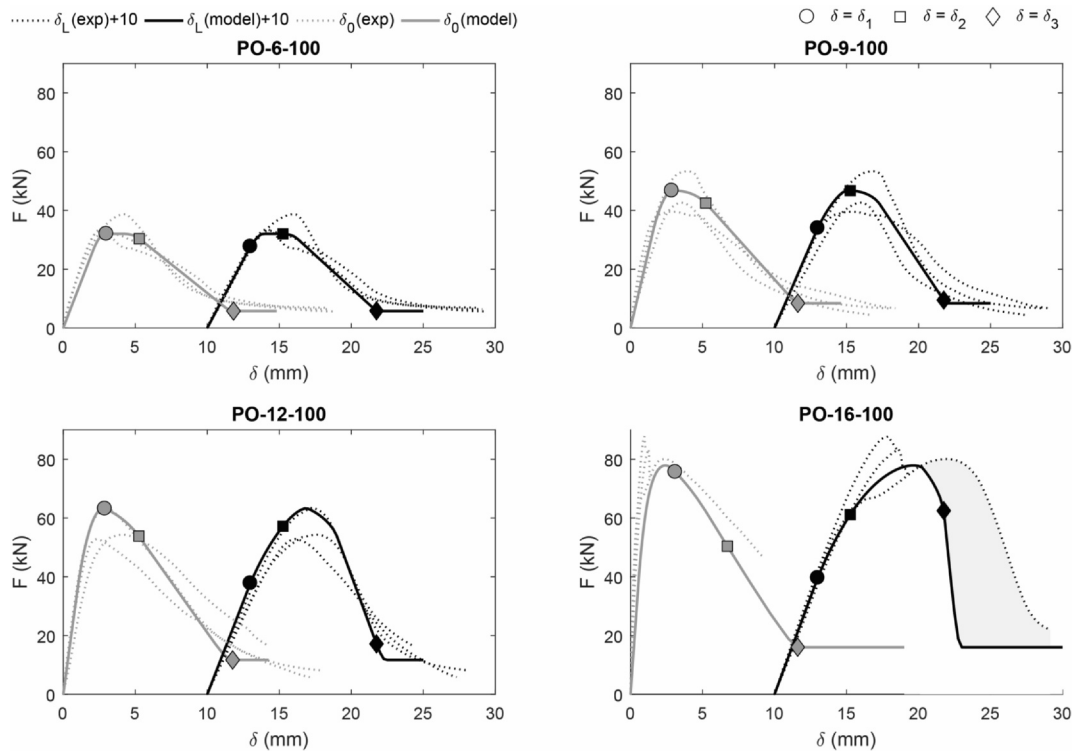
Fig. 28. Comparison results model with experimental outcomes. For clarity the loaded-end slip is presented with an initial offset of 10 mm. The end of the elastic (δ_1), damage initiation (δ_2) and damage development (δ_3) zones from the interfacial constitutive law are highlighted with circles, squares and diamonds respectively.

6. Comparison with stiff-adhesive systems

Past experimental research into the bond between FRP retrofit of masonry has focused predominantly on externally bonded plates and to a lesser degree NSM plates [27,29]. To the authors' knowledge, no tests have been previously undertaken using the deep-mounted arrangement.

The NSM arrangement, in which the FRP plate is embedded just below the surface of the masonry, provides the closest basis for comparisons to the deep-mounted FRP configuration adopted in the current work, as the strip is laterally confined in both cases.

From the database reported in Vaculik et al. [29] and supplemented with recent work [20], a total of 124 tests on the NSM retrofit of clay
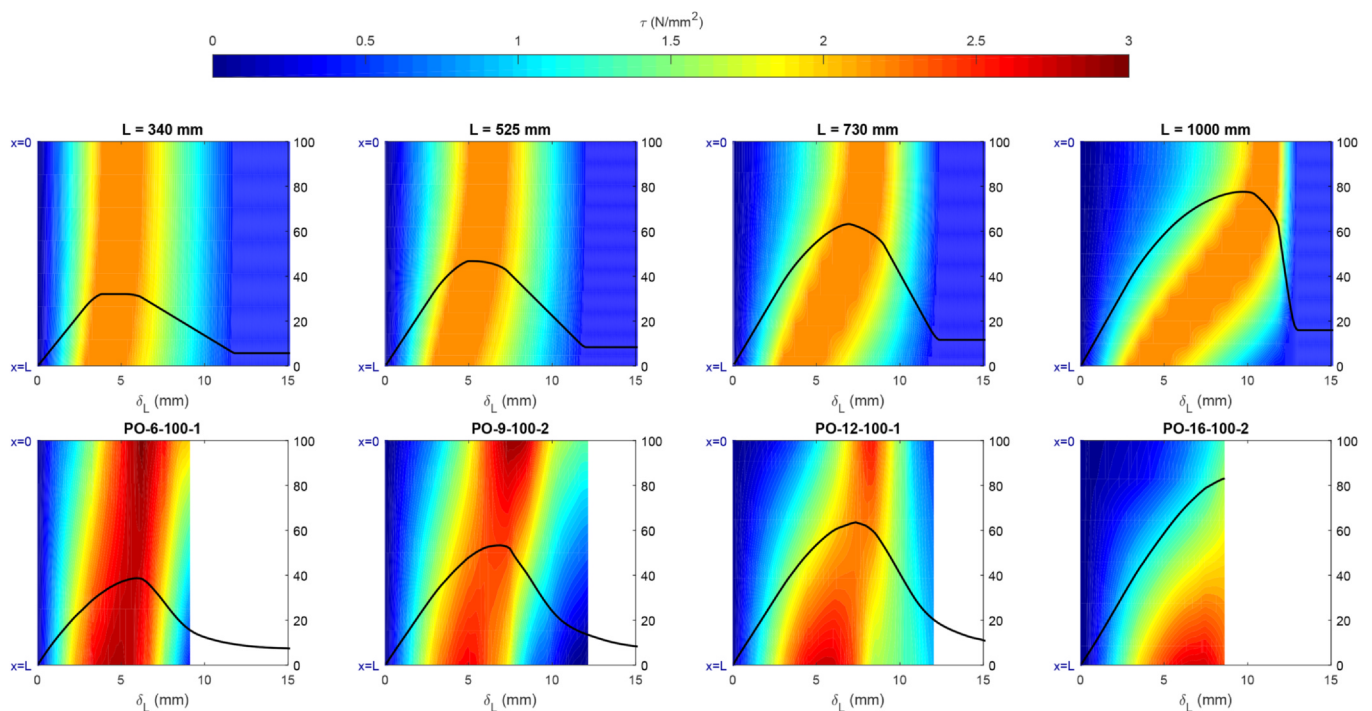

Fig. 29. Modelled (top row) and experimentally obtained (bottom row) contour plots of the local bond development over the embedded length, as a function of the loaded-end slip. Black curves shows the pull-out load.
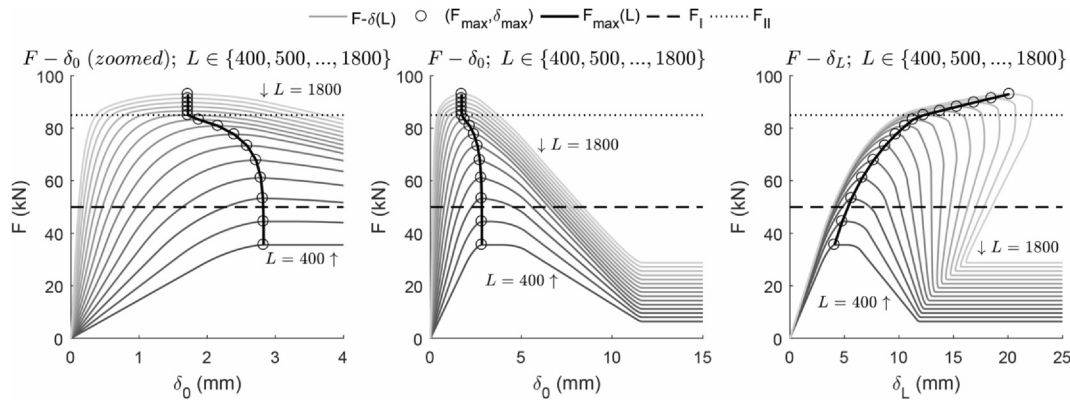
Fig. 30. $F - \delta$ relations for various anchorage lengths.

brick substrates were compiled across six separate studies [17,21,32,16,6]. These tests share the following features:

- All used conventional, stiff adhesives (two-part epoxy);
- All used rectangular CFRP strips;
- Only the tests by Maljaee et al. [20] used individual-brick prisms; the remainder all used masonry prisms comprising bricks and mortar joints, same as the current study.

In contrast to the present study where failure occurred mainly by cohesive failure of the adhesive, the predominant mode of failure observed in the NSM stiff-adhesive tests was cohesive debonding in the masonry substrate, occurring in over 80% of tests. In the remaining tests, failure occurred either by sliding at the FRP-to-adhesive interface or rupture of the FRP. A comparison of the maximum force achieved in the respective studies is shown in Fig. 34a. As the dimensions of the plate varied among the different studies ($A_p = 12$–72 mm^2), Fig. 34b demonstrates the retrofit efficiency in terms of the ultimate force per unit area of the plate (i.e. plate stress). It is seen that at the longest bonded length of 1000 mm, the flexible-adhesive system achieves both the largest load and stress among the tests considered.

6.1. Bond-slip behavior

Each of the NSM/stiff-adhesive studies that used masonry prisms [17,21,32,16,6] extracted the local bond-slip properties using the strain gauge approach. In each case, the bond-slip behavior was idealized as bilinear and ignored any residual friction (τ_r) that may have been present. The range of reported bond-slip properties is summarized in Table 5.

In Fig. 35, the bilinear bond-slip relationships reported for stiff-adhesive retrofits are compared graphically to the flexible-adhesive system in the present study. The latter is represented using both a tri-linear and bilinear ($\delta_1 = \delta_2$ in Fig. 25) idealization. To benchmark the
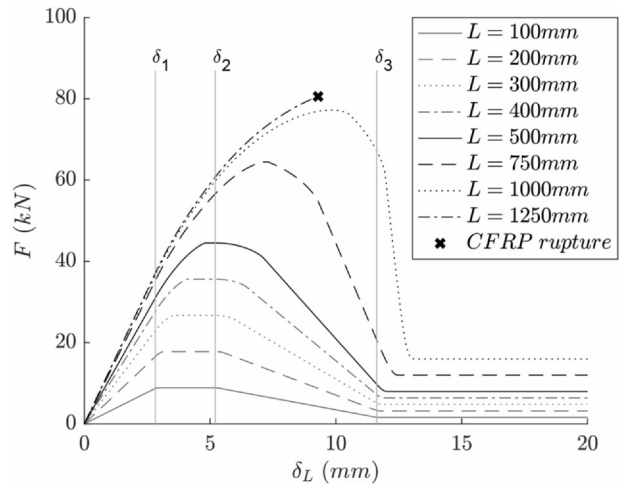

Fig. 32. Force versus loaded-end slip relation following from the partial-interaction analysis, for various anchorage lengths. CFRP strip rupture is marked with an 'x'.

stiff-adhesive system behavior against the masonry mechanical properties in the current study, the expected bond-slip behavior was predicted using the model by Kashyap et al. [16], and is plotted in Fig. 35 as a dashed line. These predictions are based on Eqs. (12) and (13).

$$\tau_f = c \cdot 8.83 \varphi_f^{0.15} f_{fl}^{0.2} \tag{12}$$

$$\delta_f = c \cdot 0.45 \varphi_f^{0.23} f_{fl}^{0.74} \tag{13}$$

where φ_f is the depth-to-width aspect ratio of the failure plane, f_{fl} is the flexural tensile strength of the substrate (modulus of rupture), and c is a correction factor taken as 0.84 to provide better fit between the model and the current experimental database [29]. The correction factor c was
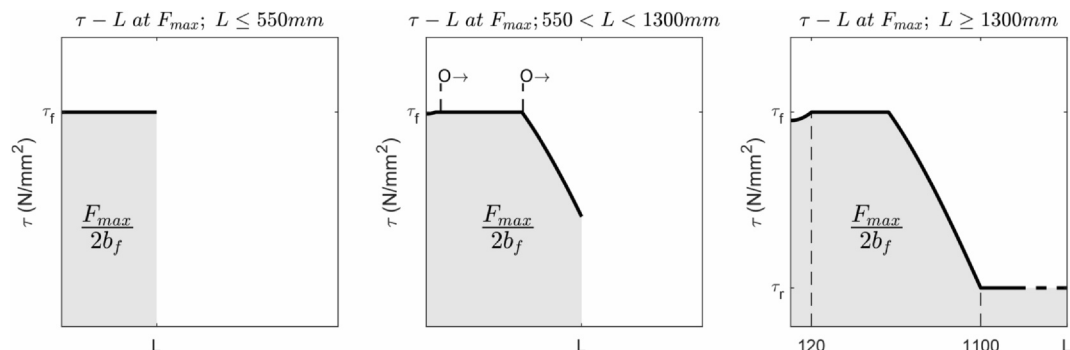

Fig. 31. Shear stress distribution corresponding to the pull-out strength.
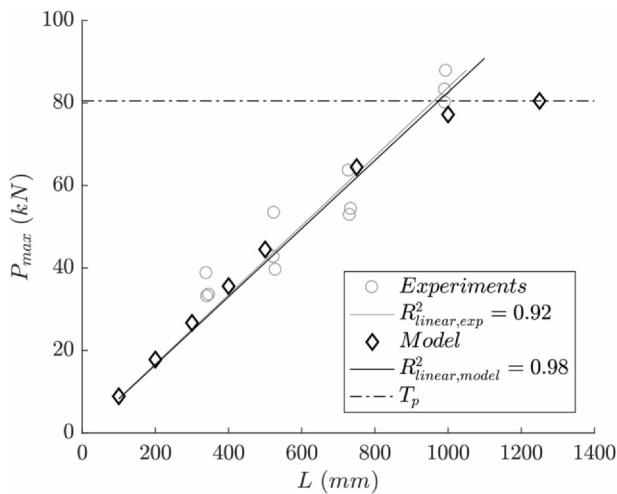
Fig. 33. Pull-out strength versus the bonded length, predicted using the partial-interaction analysis. The end of the elastic (δ_1), damage initiation (δ_2) and damage development (δ_3) zones from the interfacial constitutive law are highlighted.

tuned by re-calibrating the model proposed by Kashyap et al. [16] using the more recent and extensive experimental database of NSM tests reported in Vaculik et al. [29], to provide better agreement between the measured and predicted P_{max} values. This re-calibration was simplified in that only the factor c as presented *in Eqs. (12) and (13)* was calibrated, and the other factors and exponents in these equations were kept as per Kashyap et al. [16] original values. This is tantamount to re-calibrating the fracture energy (product of τ_f and δ_f), while keeping the critical length (resulting from the quotient δ_f / τ_f) as per the original calibration.

In the predictions f_{fl}, was calculated using the formula $f_{fl} = 0.53\sqrt{f_c}$ as used in Kashyap et al. [16]. The predicted bond-slip behavior is comparable to that reported in the individual test studies as seen in Fig. 35.

The main observations are:

- The stiff-adhesive systems achieved considerably higher peak shear stress, τ_f, (8.2–16.5 N/mm^2) than the flexible-adhesive system in the present study (2.2 N/mm^2). This can be explained by the fact that in the flexible-adhesive tests, the mechanism of local bond stress transfer was limited by the cohesive strength of the adhesive, whereas in the stiff-adhesive tests the adhesive was sufficiently strong so that failure was governed by the cohesive strength of the

brick units. This is consistent with the mode of failure generally observed in the respective tests.

- Conversely, the flexible-adhesive system achieved a much larger ultimate debonding slip of 11.6 mm compared to 0.68–2.0 mm for the stiff-adhesive systems.
- Despite having a lower τ_f, the flexible-adhesive system was still able to achieve an overall higher fracture energy, G_f, (16.9 N/mm) than the stiff-adhesive systems. For the latter, the reported fracture energy ranges from 5.3 to 15 N/mm with a mean value of 9.7 N/mm. Importantly, the debonding force that can be developed over a sufficiently long bonded length is controlled by the G_f term rather than the peak stress τ_f, through the Eq. (14), which is based on partial-interaction theory (e.g. [11]).

$$F_u^\infty = \sqrt{2G_f E_p A_p L_{\text{per}}} \tag{14}$$

where L_{per} is the perimeter of the failure plane and other variables as defined previously.

The contrasting local behavior of the flexible-adhesive system in the present study (low τ_f, high δ_3) versus stiff-adhesive systems (high τ_f, low δ_3), means that the critical bonded length (L_{crit}) needed to achieve the full debonding force is much longer for a flexible system. This is evident from the closed-form solution for L_{crit} given by Eq. (15), which is 'exact' for an idealized linear-descending ($\delta_1 = \delta_2 = 0$) bond-slip with zero residual stress (e.g. [11]), where it is seen that the ratio δ_3/τ_f is the controlling parameter.

$$L_{\text{crit}} = \frac{\pi}{2}\sqrt{\frac{\delta_3}{\tau_f} \cdot \frac{E_p A_p}{L_{\text{per}}}} \tag{15}$$

6.2. Force-slip behavior

A comparison of flexible-adhesive versus stiff-adhesive systems in terms of predicted global force-slip behavior is provided in Fig. 36. Both sets of predictions assume an identical retrofit configuration to the current study in terms of plate arrangement and bonded lengths, but differ in their local bond-slip properties. In each case, the τ-δ relationship is modelled as bilinear with a residual friction component: the flexible-adhesive system was modelled with $\tau_f = 2.63$ N/mm^2, $\delta_3 = 11.6$ mm, $\delta_1 = 4.0$ mm, and $\tau_r = 0.4$ N/mm^2 as a bilinear representation of the multi-linear rule fitted in Fig. 35; and the stiff-adhesive system with $\tau_f = 12.2$ N/mm^2, $\delta_3 = 1.30$ mm, $\delta_1 = 0.31$ mm, and $\tau_r = 0.4$ N/mm^2, where τ_f and δ_f were obtained using the Kashyap model [Eqs. (12) and (13)], and δ_1 was obtained by taking the initial slope $k_1 = 40$ N/mm^3 (Table 5). The force-slip solutions plotted in Fig. 36 were computed using the method described in Vaculik et al.
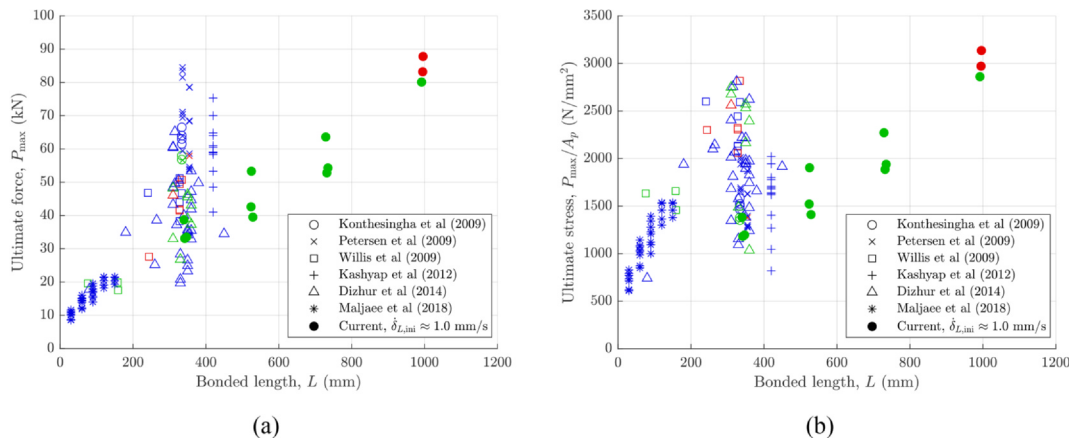

Fig. 34. Comparison of stiff-adhesive NSM tests to the present study in terms of the ultimate strength versus the bonded length: (a) ultimate force, (b) ultimate plate stress. Color denotes mode of failure: blue = cohesive debonding in the brick substrate, green = adhesive failure, red = FRP rupture. (For interpretation of the references to color in this figure legend, the reader is referred to the web version of this article.)

Table 5
Bond-slip properties for NSM retrofits of clay brick masonry prisms strengthened with CFRP strips by means of stiff adhesives (see Fig. 32). Properties τ_f, δ_1 and δ_3 were obtained from the respective sources, and from these, the fracture energy (G_f) and initial slope (k_1) were calculated. Uniaxial compressive strength (f_c) and flexural tensile strength (f_{fl}) of the brick units are also provided for comparison.

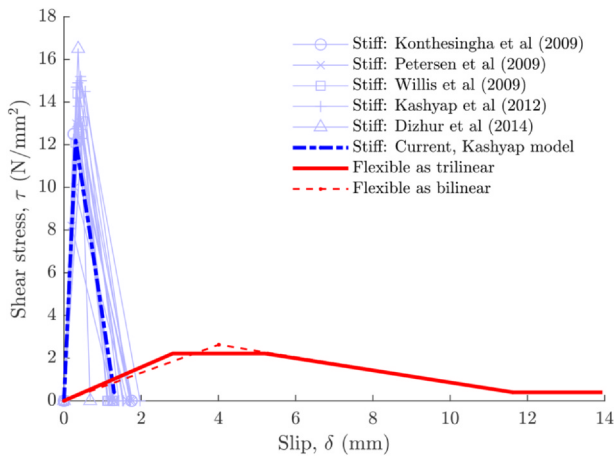|	τ_f (N/mm²)	$\delta_1(=\delta_2)$(mm)	δ_3 (mm)	G_f (N/mm)	k_1 (N/mm³)	f_c(N/mm²)	f_{fl} (N/mm²)
Konthesingha et al. [17]	12.5	0.25	1.75	10.9	50	–	3.57
Petersen et al. [21]	8.2–13.1	0.2–0.4	1.22–1.77	5.3–11.6	33–41	–	3.57
Willis et al. [32]	12.1–14.4	0.30–0.49	1.12–1.30	7.3–9.0	25–41	–	4.74
Kashyap et al. [16]	13.8–15.2	0.32–0.55	1.42–1.97	10.5–15.0	26–46	–	3.41
Dizhur et al. [6]	16.5	0.37	0.68	5.6	45	17.1	2.60

Fig. 35. Comparison of the local bond-slip behavior of the stiff-adhesive NSM systems to the flexible-adhesive system in the current study.

(2017).

The full debonding force F_u^∞ calculated using Eq. (14) is 63.9 kN for the stiff system and 88.7 kN for the flexible system. Additionally, the critical bond length, L_{crit}, for a bilinear-frictional system was calculated in accordance with the definition and method provided in Vaculik et al. (2017) as 171 mm (equivalent to a 2.7 brick-tall prism) and 1200 mm (21 brick prism) for stiff and flexible adhesive systems, respectively.

These comparisons demonstrate that flexible adhesives are a viable alternative to conventional stiff adhesives for FRP strengthening of masonry. Among the indicated advantages of using a flexible-adhesive system with respect to out-of-plane wall strengthening are:

- Higher interfacial fracture energy G_f leading to increased wall strength capacity;
- Increased wall displacement capacity arising from higher local slip capacity δ_3; and

- Larger slip capacity at damage initiation, δ_1, leading to increased wall displacement capacity at the onset of irreversible damage to the retrofit.

7. Conclusions and future work

An experimental program was undertaken to assess the high-speed pullout behavior of deep-mounted CFRP strips bonded with a flexible, visco-elasto-plastic adhesive to clay brick masonry. The direct pull-out test was used for the evaluation of the bond-slip behavior of the embedded CFRP strips. From the experimental campaign the following conclusions can be drawn:

1) Increasing the machine displacement rate from 0.5 mm/min ($\dot{\delta}_{L,ini} \approx 0.004$ mm/s)to 100 mm/min ($\dot{\delta}_{L,ini} \approx 1.0$ mm/s) led to an increase of 67% in pull-out strength for an embedment length of ~1 m. A strong logarithmic correlation ($R^2 = 0.93$) was found for the relation between strength and displacement rate. Additionally the governing failure mechanism shifted from cohesive failure to CFRP strip rupture. The latter was applicable to two of the three specimens with an embedment length of ~1 m.

2) Testing the pull-out behaviour of systems that include visco-elasto-plastic components should be conducted at a loading rate that is representative for the practical application of the system.

3) Keeping the machine displacement rate constant at 100 mm/min ($\dot{\delta}_{L,ini} \approx 1.0$ mm/s)and reducing the embedment length, shifted the governing failure mechanism from CFRP strip rupture ($L \approx 1$ m) to cohesive failure in the adhesive ($L < 1$ m). A very strong linear correlation ($R^2 = 0.92$) was found for the relation between embedment length and pull-out strength, up to the critical embedment length of ~1 m.

4) Brick splitting was observed when the CFRP/adhesive interface entered the damage initiation phase. For specimens that were governed by cohesive failure, the complete specimen showed splitting. For the specimens that underwent CFRP rupture, the splitting was limited to the bonded length where the CFRP/adhesive interface
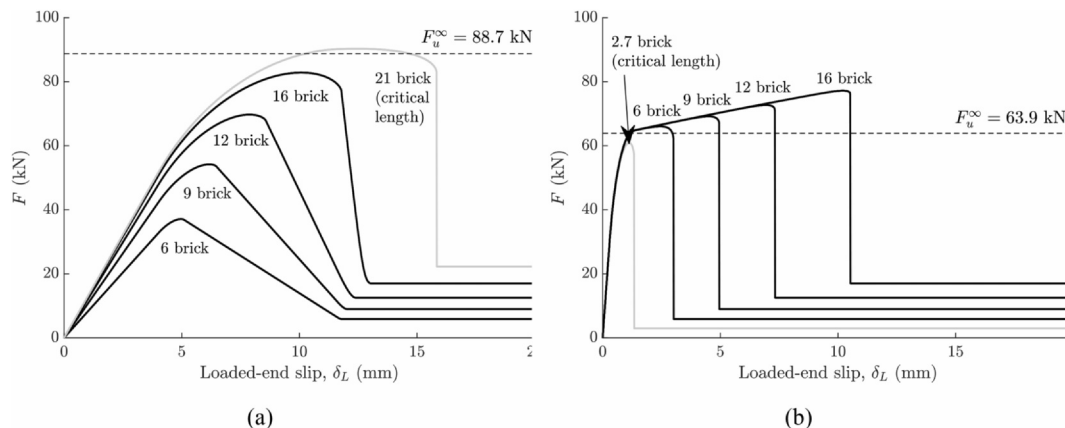

Fig. 36. Comparison of theoretical force-slip behavior of: (a) flexible-adhesive, and (b) stiff-adhesive systems.

entered the damage initiation phase.

5) The increase in local bond strength towards the free end of the specimen was attributed to the non-uniform slip rate throughout the experiment. The slip-rate was disrupted by the finite stiffness of the machine, the threaded rods (used to connect the restraint plate to the base of the machine) and the CFRP strip between the masonry and the grips of the machine. The relaxation of the aforementioned elements during the post-peak region caused a significant noise in the slip rate over the entire embedment length, in particular at the free-end side.

6) Based on the readings of the strain gauges on the embedded CFRP strip, multiple tri-linear local bond-slip relations were obtained for specimens that were subjected to 100 mm/min machine displacement rate. The separate bond-slip relations were averaged to obtain a universal local bond-slip law. For the averaged tri-linear local bond-slip behavior the interfacial fracture energy was determined at 16.9 N/mm.

7) Using the averaged multi-linear local bond-slip model as a part of a partial-interaction analysis led to a good agreement with experimental results for embedment lengths 0.34 m, 0.53 m and 0.73 m. For an embedment length of ~1.0 m, the agreement was good for the pre-peak phase. In the post-peak phase, the proposed model showed a reduced post-peak behavior and stronger decline when compared to the experimental results. This deviation was attributed to the non-uniform slip rate during the experiment.

Additionally, a comparison was made between the system tested in this research and a database consisting of 124 tests on near-surface-mounted (NSM) retrofits of clay brick substrates using a conventional stiff adhesive. From this comparison, considering both bond-slip and force-slip behavior, the following conclusions can be drawn:

8) Stiff-adhesive systems were able to achieve considerably higher peak shear stresses (8.2–16.5 N/mm^2) than for the flexible-adhesive system used in the present study (2.2 N/mm^2). Conversely, the flexible-adhesive system achieved a much larger ultimate debonding slip of 11.6 mm compared to 0.68–2.0 mm for the stiff-adhesive systems. Despite having a lower peak bond stress, the flexible-adhesive system was still able to achieve an overall higher fracture energy (16.9 N/mm) than the stiff-adhesive systems (9.7 N/mm).

9) The debonding force that can be developed over a sufficiently long bonded length is controlled by the fracture energy (flexible adhesive) rather than the peak stress (stiff adhesive). The estimated critical bond length is 1200 mm (equivalent to a 21 brick prism) for the flexible-adhesive system tested, and 171 mm (equivalent to a 2.7 bricks long prism) for an equivalent retrofit with stiff adhesive; which agrees well with the experiment.

As for the future work, firstly it is important to validate the claim regarding the non-uniform slipping rate causing a significant deviation between the model and experimental results. Additional pull-out experiments will be conducted, where the loading rate is controlled in terms of the loaded-end slip rate instead of the machine displacement rate. Secondly, finite element modelling will provide more insight in the stresses that initiate the splitting of the bricks. Finally, research will be conducted on the effectiveness of the bond-slip relations obtained in this study, in combination with a three-hinge rigid-body model, to model the out-of-plane behavior of a reinforced masonry wall. This will be done by means a large-scale out-of-plane experimental program.

Declaration of Competing Interest

The authors declare that they have no known competing financial interests or personal relationships that could have appeared to influence the work reported in this paper.

Acknowledgements

References

[1] Adams DO, Adams DF. Tabbing guide for composite test specimens (No. DOT/FAA/AR-02/106). UTAH UNIV SALT LAKE CITY DEPT OF MECHANICAL ENGINEERING; 2002.

[2] ASTM. ASTM C67-03a, standard test methods for sampling and testing brick and structural clay tile. ASTM International, Conshohocken, PA; 2003.

[3] ASTM. C1006-07: standard test method for splitting tensile strength of masonry units, 2007. ASTM International, West Conshohocken, PA; 2007.

[4] Ceroni F, Darban H, Luciano R. Analysis of bond behavior of injected anchors in masonry elements by means of Finite Element Modeling. Compos Struct 2020:112099. https://doi.org/10.1016/j.compstruct.2020.112099.

[5] Dizhur D, Ingham J, Moon L, Griffith M, Schultz A, Senaldi I, … Ventura C. Performance of masonry buildings and churches in the 22 February 2011 Christchurch earthquake. Bull N Z Soc Earthq Eng 2001;44(4):279–296.

[6] Dizhur D, Griffith MC, Ingham JM. Pullout strength of NSM CFRP strips bonded to vintage clay brick masonry. Eng Struct 2014;69:25–36.

[7] European Committee for Standardization. EN 1052-1:1999: Methods of test for masonry—part 1: determination of compressive strength. European Committee for Standardization, Brussels, Belgium; 1999.

[8] European Committee for Standardization. EN 1015-11:1999/A1:2007: Methods of test for mortar for masonry—part 11: determination of flexural and compressive strength of hardened mortar. European Committee for Standardization, Brussels, Belgium; 2007.

[9] European Committee for Standardization. EN 772-1:2011/A1:2015: methods of test for masonry units—part 1: determination of compressive strength. European Committee for Standardization, Brussels, Belgium; 2015.

[10] Griffith MC, Kashyap J, Mohamed Ali MS. Flexural displacement response of NSM FRP retrofitted masonry walls. Constr Build Mater 2013;49:1032–40.

[11] Haskett M, Oehlers DJ, Mohamed Ali MS. Local and global bond characteristics of steel reinforcing bars. Eng Struct 2008;30(2):376–83.

[12] Ianniruberto U, Rinakdi Z. Influence of FRP reinforcement on the local ductility of RC elements. In: FRP Composites in Civil Engineering. Proceedings of the International Conference on FRP composites in Civil EngineeringHong Kong Institution of Engineers, Hong Kong Institution of Steel Construction, vol. 1; 2001.

[13] Ingham J, Griffith M. Performance of unreinforced masonry buildings during the 2010 Darfield (Christchurch, Nz) Earthquake. Aust J Struct Eng 2010;11(3):207–24.

[14] ISO. 11003-2. Adhesives – Determination of shear behaviour of structural bonds, Part 2: Thick-adherend tensile-test method; 1993.

[15] ISO. 527-1. Plastics. Determination of tensile properties. Part, 1; 2012.

[16] Kashyap J, Willis CR, Griffith MC, Ingham JM, Masia MJ. Debonding resistance of FRP-to-clay brick masonry joints. Eng Struct 2012;41:186–98.

[17] Konthesingha KMC, Masia MJ, Petersen RB, Page AW. Bond behaviour of NSM FRP strips to modern clay brick masonry prisms under cyclic loading. In: Proc., 11th Canadian Masonry Symposium; 2009.

[18] Kortekaas M, Jaarsma B. Improved definition of faults in the Groningen field using seismic attributes. Neth J Geosci 2017;96(5):s71–85.

[19] Kwiecień A. Stiff and flexible adhesives bonding CFRP to masonry substrates—Investigated in pull-off test and Single-Lap test. Arch Civ Mech Eng 2012;12(2):228–39.

[20] Maljaee H, Ghiassi B, Lourenço PB. Bond behavior in NSM-strengthened masonry. Eng Struct 2018;166:302–13.

[21] Petersen RB, Masia MJ, Seracino R. Bond behavior of near-surface mounted frp strips bonded to modern clay brick masonry prisms: influence of strip orientation and compression perpendicular to the strip. J. Compos. Constr. 2009;13(3):169–78.

[22] Sturm AB, Visintin P, Vaculik J, Oehlers DJ, Seracino R, Smith ST. Analytical approach for global load-slip behaviour of FRP plates externally bonded to brittle substrates with anchors. Compos B Eng 2019;160:177–94.

[23] Torre-Casanova A, Jason L, Davenne L, Pinelli X. Confinement effects on the steel–concrete bond strength and pull-out failure. Eng Fract Mech 2013;97:92–104.

[24] Türkmen ÖS, Wijte SNM, Vermeltfoort AT, Martens DRW. Experiments to determine the out-of-plane behavior of CFRP and ductile adhesive reinforced clay brick masonry walls. In: 13th Canadian Masonry Symposium, July 4–7, 2017, Halifax, Canada; 2017. p. 1–11).

[25] Türkmen ÖS, Wijte SNM, Ingham JM, Vermeltfoort AT. Bond slip behaviour of deep mounted carbon fibre reinforced polymer strops confined with a ductile adhesive in clay brick masonry. In: Proceedings of 10th Australasian masonry conference: masonry today and tomorrow, blz; 2018. p. 672–86.

[26] Triantafillou TC. Strengthening of masonry structures using epoxy-bonded FRP laminates. J Compos Constr 1998;2(2):96–104.

[27] Vaculik J, Visintin P, Burton NG, Griffith MC, Seracino R. State-of-the-art review and future research directions for FRP-to-masonry bond research: test methods and techniques for extraction of bond-slip behaviour. Constr Build Mater

2018;183:325–45.

[28] Vaculik J, Sturm AB, Visintin P, Griffith MC. Modelling FRP-to-substrate joints using the bilinear bond-slip rule with allowance for friction—Full-range analytical solutions for long and short bonded lengths. Int J Solids Struct 2018;135:245–60.

[29] Vaculik J, Visintin P, Burton NG. Global database of FRP-to-masonry bond strength tests. Data Brief 2018;20:2065–71.

[30] Vaculik J, Visintin P, Lucas W, Griffith MC. Durability of near-surface-mounted FRP-to-clay brick masonry retrofits under environmental exposure. J Compos Constr 2020;24(1). https://doi.org/10.1061/(ASCE)CC.1943-5614.0000997.

[31] Wijte SNM, Türkmen ÖS, Vermeltfoort AT, Martens DRW. Analytical modelling of the out-of-plane behavior of CFRP and ductile adhesive reinforced clay brick masonry walls. In: 13th Canadian Masonry Symposium, July 4–7, 2017, Halifax, Canada; 2017.

[32] Willis CR, Yang Q, Seracino R, Griffith MC. Bond behaviour of FRP-to-clay brick masonry joints. Eng Struct 2009;31(11):2580–7.